

Effect of parasitic capacitance and inductance on the dynamics and noise of dc superconducting quantum interference devices

Cite as: Journal of Applied Physics **71**, 6150 (1992); <https://doi.org/10.1063/1.350424>

Submitted: 06 January 1992 • Accepted: 25 February 1992 • Published Online: 04 June 1998

Tapani Ryhänen, Heikki Seppä and Robin Cantor



View Online



Export Citation

ARTICLES YOU MAY BE INTERESTED IN

CURRENT-VOLTAGE CHARACTERISTICS OF JOSEPHSON JUNCTIONS

Applied Physics Letters **12**, 277 (1968); <https://doi.org/10.1063/1.1651991>

Ultra-low-noise tunnel junction dc SQUID with a tightly coupled planar input coil

Applied Physics Letters **40**, 736 (1982); <https://doi.org/10.1063/1.93210>

The inductance of a superconducting strip transmission line

Journal of Applied Physics **50**, 8129 (1979); <https://doi.org/10.1063/1.325953>



Webinar
Quantum Material Characterization
for Streamlined Qubit Development



Register now

Effect of parasitic capacitance and inductance on the dynamics and noise of dc superconducting quantum interference devices

Tapani Ryhänen^{a)} and Heikki Seppä

Metrology Research Institute, Helsinki University of Technology, and Technical Research Centre of Finland, 02150 Espoo, Finland

Robin Cantor

Physikalisch-Technische Bundesanstalt, Institut Berlin, Abbestrasse 10-12, W-1000 Berlin 10, Germany

(Received 6 January 1992; accepted for publication 25 February 1992)

Practical thin-film dc superconducting quantum interference devices (SQUIDs) are often built with an integrated input coil which leads to the formation of various parasitic elements. We have designed and fabricated several square washer-shaped dc SQUID test devices with various amounts of parasitic capacitance formed by covering the washer slits with superconducting coverplates of various widths. In the simplest approximation, the parasitic capacitance C_p appears entirely across the Josephson junctions; in a better approximation, C_p divides the total inductance into two parts, an effective SQUID loop inductance L and a small parasitic inductance L_p . For both models, noise-free and noise-rounded current-voltage and voltage-flux characteristics are calculated for various values of the ratios L/L_p and C_p/C , where C is the Josephson junction capacitance. The SQUID dynamics are significantly affected by C_p and L_p . The energy resolution ϵ at first deteriorates with increasing C_p for $C_p/C \lesssim 2$, but as C_p/C becomes large, ϵ improves to less than twice the value for $C_p/C \approx 0$. The optimal points of operation for large C_p however, are found at voltages above the low-frequency resonance determined by L and C_p where the flux-to-voltage transfer function is low. Furthermore, for devices with $C_p/C \gg 1$ and $L_p \neq 0$, the double-loop geometry leads to an additional resonance determined by L_p and C that appears at high frequencies. The energy resolution inside this high-frequency resonance is nearly independent of C_p and comparable to the energy resolution of a device having the same total inductance but with $C_p/C \ll 1$. Extensive noise mappings on several different test devices have been carried out using a computer-controlled measurement system. The measured characteristics and noise performance are shown to be in good agreement with the simulations.

I. INTRODUCTION

An important figure of merit for dc superconducting quantum interference devices (SQUIDs) is the noise energy per unit bandwidth, commonly referred to as the energy resolution. Several uncoupled dc SQUIDs with energy resolutions approaching the quantum limit at 4.2 K are reported in the literature.¹⁻⁴ A practical thin-film dc SQUID with an integrated input coil, however, is generally more noisy because the SQUID inductance cannot be made arbitrarily small if adequate coupling is to be maintained. In addition, the integration of the input coil on top of the SQUID loop creates several parasitic elements: A parasitic capacitance is introduced which shunts the SQUID loop, a microstripline is formed by the input coil with the SQUID loop as ground plane, and, depending on the layout, a sizable parasitic inductance may be created.

Capacitive shunting of the SQUID loop has been discussed from two seemingly contradictory points of view: as an intentionally introduced feature to improve coupling, and more recently, as an unwanted parasitic effect which causes a deterioration of the energy resolution. Following a scheme first used by Hollenhorst and Giffard for rf

SQUID's,^{5,6} Paik, Mathews, and Castellano⁷ developed a toroidal point contact dc SQUID with a capacitive shunt that divides the total SQUID inductance into two parts: a high "coupling" inductance and a low effective "SQUID" inductance. The idea behind such a double-loop geometry is that the low-frequency coupling to the SQUID is improved, whereas at the much higher Josephson frequencies, the effective SQUID inductance is much lower. Thus, the overall performance of the device should be enhanced. Tesche⁸ performed a detailed analysis of the double-loop dc SQUID and found that the energy resolution is approximately equal to that of a conventional dc SQUID with the same total loop inductance and junction parameters. The analysis also indicates that the optimal point of operation for the double-loop geometry occurs for a bias current much higher than the SQUID critical current, whereas for a conventional dc SQUID the optimum bias current is very near the SQUID critical current. Tesche *et al.*⁹ later fabricated a coupled dc SQUID with double-loop geometry, the capacitive shunt arising from the presence of a slit ground-plane and a 78-turn integrated input coil. The SQUID characteristics at low-bias currents show irregularities, and the optimal energy resolution, measured in an open-loop mode at high-bias currents as expected, is an order of magnitude higher than that predicted for a conventional dc

^{a)}Present address: Vaisala Technologies, Inc., PL 9, SF-00421 Helsinki, Finland.

SQUID with the same total inductance. Drung *et al.*¹⁰⁻¹² have recently described a direct-coupled, high-inductance SQUID magnetometer without an input coil. The minimum energy resolution of this device, measured in a flux-locked mode at high-bias currents, is about a factor of 2-3 higher than that predicted for a conventional dc SQUID with the same total inductance.

On the other hand, computer simulations¹³⁻¹⁵ indicate that capacitive shunting of the SQUID loop affects the performance. In general, the parasitic capacitance and the other parasitic elements introduced by the presence of the input coil lead to resonances which couple to the SQUID dynamics;¹⁶⁻²⁵ the SQUID characteristics become irregular and exhibit resonance steps, making operation of the electronics difficult. The development of practical dc SQUIDs with integrated input circuits, therefore, requires an understanding of the influence of these parasitic elements on the dynamics. In particular, a model is needed which can predict the performance of design prototypes.

Procedures for the design of practical, ultralow noise dc SQUIDs have recently been described^{14,20,22} which take the parasitic effects introduced by the input coil into account. The SQUID layout and electrical parameters are chosen so that the amount of parasitic capacitance is less than the junction capacitance and the possible microwave resonances are well away from the desired point of operation. In addition, the microwave transmission line resonances are damped by a series RC shunt¹⁴ in parallel with the input coil. Knuutila, Ahonen, and Tesche²⁶ have demonstrated that the use of an RC shunt smooths the characteristics of the IBM double-loop SQUID⁹ and enables flux-locked-loop operation at lower bias currents where the flux-to-voltage transfer function is higher with a significant improvement in performance. The characteristics of more recent devices^{22,27} built according to these design procedures are smooth and the energy resolutions are close to the values predicted for the corresponding conventional, uncoupled dc SQUID's.

Alternatively, the insertion of a damping resistor across the SQUID loop inductance is seen experimentally to smooth the irregular characteristics.^{10,28-30} Numerical simulations by Foglietti *et al.*²⁹ indicate that the additional damping resistor does not significantly contribute to the flux noise if the resistance is of the same order as the junction shunt resistance. Enpuku *et al.*³¹ have numerically analyzed the effect of the damping resistor on SQUID performance and point out that devices with the damping resistor can be designed for large $\beta_L = 2\pi LI_c/\Phi_0$, thereby enhancing the coupling properties of the SQUID without significant loss in resolution. The effect of the damping resistor on the SQUID dynamics, however, has not been investigated.

In an earlier report,²³ we presented preliminary results on the effect of the parasitic capacitance C_p on dc SQUID characteristics. In that report, measurements on several square-washer-shaped dc SQUID's with varying amounts of parasitic capacitance, formed by covering the washer slit with superconducting films of various widths, are described, and simulated current-voltage characteristics, cal-

culated using a simple lumped-circuit-element model, are shown to be in very good agreement with the measured characteristics. From the numerical simulations and the measurements, the energy resolution is shown to deteriorate with increasing C_p , roughly as $\sqrt{L_{\text{tot}}(C + 2C_p)}$. Daalmans *et al.*²⁵ report similar measurements on higher inductance dc SQUID's. The irregularities in the SQUID characteristics due to C_p are shown, but the functional dependence of the energy resolution on C_p could not be determined.

In this paper, we present the results of recent computer simulations and detailed experimental measurements which more clearly show the effects of both parasitic capacitance and inductance on dc SQUID performance. The simple test device that we consider in this investigation and two lump-circuit-element models of this device are introduced in Sec. II. The numerical methods are discussed in Sec. III A and the simulated noise-free and noise-rounded current-voltage characteristics are presented in Sec. III B. The voltage-flux characteristics, flux-to-voltage transfer function, voltage noise, and the flux noise are calculated in Sec. III C. The effect of a damping resistor in parallel with the SQUID inductance is discussed in Sec. III D. The fabrication of the test devices is discussed in Sec. IV A, and the measurement setup is described in Sec. IV B. The measured characteristics and performance are presented in Sec. IV C. A discussion of the results and conclusions appear in Sec. V.

II. TEST DEVICE AND LUMPED-CIRCUIT-ELEMENT MODEL

The most commonly used planar dc SQUID geometry, first introduced by Ketchen and Jaycox^{32,33} in 1981, is a square-shaped washer with a square hole in the center and a slit from the hole to the outer edge. This defines the SQUID loop. A schematic drawing of a square-washer dc SQUID with an integrated input coil is shown in Fig. 1(a). Such a design offers excellent coupling, $k \lesssim 1$, but the input coil introduces a parasitic capacitance C_p which shunts the SQUID loop and, together with the washer as a ground plane, forms a microwave transmission line. A simple way to study the capacitive effect introduced by the input coil is shown in Fig. 1(b), where a "parasitic" capacitance is intentionally introduced by placing a wide superconducting coverplate on top of the washer slit.²³ This is the geometry of the test device used in this investigation.

The total SQUID inductance of the test device is the sum of three terms: the inductance of the washer hole, L_{hole} , the inductance of that portion of the slit that is covered, L_{cov} , and the inductance of that portion of the slit nearest to the junctions that is not covered, L_{uncov} . The hole inductance $L_{\text{hole}} \approx 1.25 \mu_0 D$, where D is the width of the square hole.³² The inductance L_{uncov} can be estimated using the experimentally observed result³⁴ that the inductance per unit length of an uncovered 3- μm -wide slit is about 0.35 pH/ μm . If the length of the slit is short compared to the wavelength of the Josephson oscillations, the covered slit can be modeled in terms of lumped-circuit inductances and capacitances. In order to estimate L_{cov}

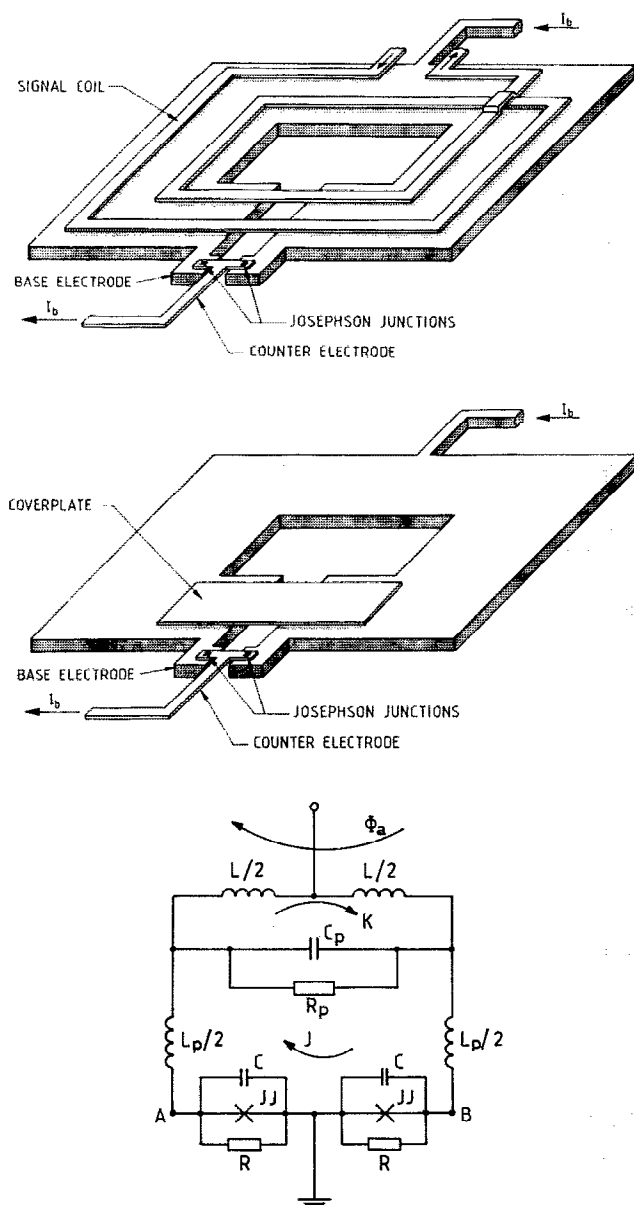


FIG. 1. (a) Schematic drawing of a square-washer dc SQUID with an integrated input coil. (b) Schematic drawing of the test device consisting of a square-washer dc SQUID with a coverplate on top of a slit, and (c) lumped-circuit-element model of the test device. Here, C , R , and I_c denote the junction capacitance, shunt resistance, and critical current, respectively. The parasitic capacitance C_p divides the total inductance into an effective SQUID loop inductance L and a parasitic inductance L_p . A damping resistor R_p is included in the model. The screening currents J and K are indicated in the figure.

and the capacitance introduced by the slit coverplate, the covered portion of the slit may be viewed as two parallel transmission lines, each with a capacitance C_l and inductance L_l per unit length. As a rough approximation, $L_{cov} \approx 2L_l l$ and $C_p \approx C_l l/2$, where l is the length of the slit. This approximation should be valid if the width of the coverplate on each side of the slit is less than the length of the slit and greater than the thickness of the insulator between the cover and the washer. This is the case for the test

devices described here. The capacitance calculated in this way is found to be in good agreement with a calculation based on the geometry.

In this paper, we consider two lumped-circuit-element models for the test devices. In the simplest approximation, the covered slit can be modeled as a single capacitance C_p and a single inductance L_{cov} . Then, C_p is assumed to appear entirely across the Josephson junctions and the total SQUID inductance $L_{tot} = L_{cov} + L_{uncov} + L_{hole}$. This approximation should be relatively good if $L_{hole} \gg L_{cov}$, L_{uncov} . As a better approximation, we model the covered slit as a T circuit consisting of the two inductances $L_{cov}/2$ and the capacitance C_p . We then define the parasitic inductance $L_p = L_{uncov} + L_{cov}/2$ and the effective SQUID inductance $L = L_{hole} + L_{cov}/2$. A lumped-circuit-element model of the test device with this T -circuit approximation for the covered slit is shown in Fig. 1(c). A damping resistor R_p in parallel with C_p is included in the model. The Josephson junctions are assumed to be identical and are represented by the resistively shunted-junction (RSJ) model,^{35,36} which consists of an ideal Josephson junction with critical current I_c and junction capacitance C shunted by a resistance R . The SQUID is biased with a current I_b , and the measured voltage across the SQUID is V . The circulating currents K and J , flowing through the inductance L and the Josephson junctions, respectively, are also shown in the figure.

The lumped-circuit-element model shown in Fig. 1(c) is equivalent to the model used by Tesche⁸ for the double-loop dc SQUID. In Tesche's analysis,⁸ the heavily overdamped case ($\beta_c \approx 0$) is considered. We show in Sec. III that an additional feature appears in the SQUID dynamics for $\beta_c \neq 0$. Although the lumped-circuit-element model should be a reasonable approximation for a coupled dc SQUID with a covered slit, the distribution of the parasitic capacitance and inductance for the geometry shown in Fig. 1(a) is probably more complicated.^{37,38}

We now turn to a discussion of the differential equations for the lumped-circuit-element model shown in Fig. 1(c). If we use the variables $v = (\delta_1 + \delta_2)/2$ and $\varphi = (\delta_1 - \delta_2)/2$, where δ_1 and δ_2 are the phase differences across the junctions, and the normalized time t^* in units of $\Phi_0/(2\pi R I_c)$, where Φ_0 is the flux quantum, the model leads to a set of three second-order differential equations which can be written in the following form:

$$\beta_c \frac{d^2 v}{dt^{*2}} + \frac{dv}{dt^*} + \sin v \cos \varphi = i + i_{n,v}(t^*), \quad (1)$$

$$\begin{aligned} \beta_c \frac{d^2 \varphi}{dt^{*2}} + \frac{d\varphi}{dt^*} + \cos v \sin \varphi + 2(\varphi - \varphi_a)/\beta_L \\ = k + i_{n,\varphi}(t^*), \end{aligned} \quad (2)$$

$$\begin{aligned} \eta \beta_L \frac{d^2 k}{dt^{*2}} + \rho \beta_L \frac{dk}{dt^*} + (1 + 1/\xi)k \\ = 2(\varphi - \varphi_a)/\beta_L + i_{n,damp}(t^*), \end{aligned} \quad (3)$$

where $i = I_b/2I_c$ is the normalized current through the SQUID, $k = LK/L_p I_c$ is the normalized current circulat-

ing in the loop formed by the large inductance L , $\varphi_a = \pi\Phi_a/\Phi_0$ is the normalized applied flux, and the dimensionless parameters $\beta_L = 2\pi LI_c/\Phi_0$, $\beta_c = 2\pi R^2 C I_c/\Phi_0$, $\rho = R/R_p$, $\eta = C_p/C$, and $\xi = L/L_p$. The thermal noise is represented by the uncorrelated random variables $i_{n,v}$, $i_{n,\varphi}$, and $i_{n,damp}$ with zero mean, defined such that $\langle i_{n,v}(t^* + \tau) i_{n,v}(t^*) \rangle = \langle i_{n,\varphi}(t^* + \tau) i_{n,\varphi}(t^*) \rangle = \Gamma \delta(\tau)$, and $\langle i_{n,damp}(t^* + \tau) i_{n,damp}(t^*) \rangle = \rho \Gamma \delta(\tau)$. Here, $\Gamma = 2\pi k_B T / I_c \Phi_0$ is the normalized thermal energy. If the parasitic inductance L_p is reduced, i.e., $\xi \rightarrow \infty$, Eqs. (2) and (3) can be replaced by the single differential equation,

$$\beta_{c,eff} \frac{d^2 \varphi}{dt^{*2}} + (1 + 2\rho) \frac{d\varphi}{dt^*} + \cos v \sin \varphi + 2(\varphi - \varphi_a)/\beta_L = i_{n,\varphi}(t^*), \quad (4)$$

where $\beta_{c,eff} = (1 + 2\eta)\beta_c$.

Equations (1), (2), and (3) describe a very complicated dynamical system with three degrees of freedom which can be identified with the three independent currents I_b , J , and K . Although the three equations are coupled to each other, some insight into the dynamics can be gained by considering two special cases. The classification of the solutions to the differential equations described below will be useful for the discussion in Sec. III.

For the case $L_p = C_p = \rho = 0$, Eqs. (1) and (4) reduce to the set of two second-order differential equations²¹ describing an uncoupled dc SQUID. This case has been studied by several different authors.³⁹⁻⁴⁵ It has been pointed out^{21,44,46} that the same equations describe the motion of a classical particle in a parabolic potential "trough" with sinusoidal bumps, $U(v, \varphi) = (\varphi - \varphi_a)^2/\beta_L - iv - \cos v \cos \varphi$. The steepness of the trough is determined by β_L : as β_L increases, the trough becomes more flat. Depending on the parameters, the solutions of the differential equations describe static zero-voltage fluxoid states or finite voltage states. The zero-voltage states are characterized by the condition that $\varphi = v = \text{constant}$. Possible finite voltage states are a single-junction or "running" mode, a "beating" mode, or a coexistence of the two. In the absence of applied flux, the running mode is characterized by the condition $\varphi = 0$: there is no circulating current, the SQUID behaves like a single Josephson junction, and the dynamics depend only on β_c and the bias current i . The beating mode is characterized by oscillations with respect to φ that are symmetric about $\varphi = 0$: an oscillating circulating current exists and the dynamics depend on all three parameters β_c , β_L , and i . In the presence of applied flux, the running and beating modes become more difficult to distinguish. The beating mode, however, is always characterized by larger amplitude circulating current oscillations and a lower average voltage.

For the case $L_p = 0$ and $C_p \neq 0$, the system is described by Eqs. (1) and (4). For the classical particle analog, the effective mass ($\beta_{c,eff}$) for motion with respect to φ is now higher. For the SQUID, the increased "inertia" leads more easily to large amplitude oscillations of the circulating current: the beating mode is enhanced. For a given C_p , increasing β_c or β_L further enhances this effect. The resistance

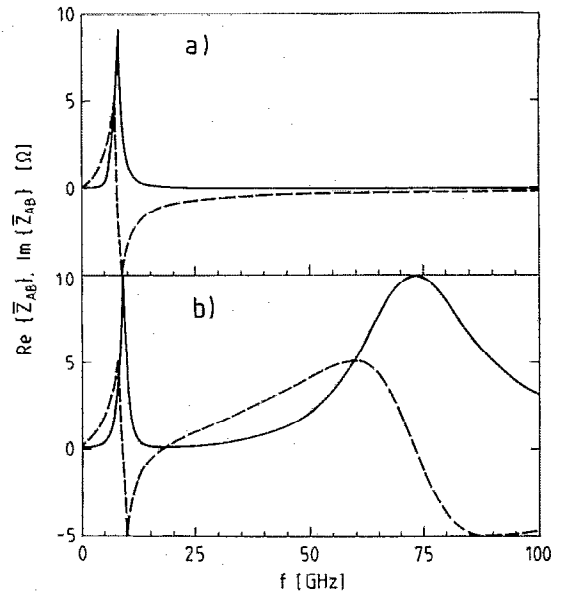


FIG. 2. Calculated real (solid line) and imaginary (dashed line) parts of the impedance Z_{AB} between points A and B of the lumped-circuit-element model shown in Fig. 1(c) for $C=1$ pF, $R=5$ Ω , $C_p=10$ pF, $L_{tot}=L+L_p=40$ pH and (a) $L_p=0$, and (b) $L/L_p=3$.

R_p across the SQUID inductance in Fig. 1(c) serves to damp this mode, as can be seen from the presence of the damping term in Eq. (4).

Most dc SQUID applications assume that the device operates only in the running mode when in the finite voltage state. We will show in Sec. III that, for reasonable values of β_L and β_c , parasitic capacitance enhances the beating mode and leads to a situation where multiple voltage states exist. Thermal noise can activate hopping between the different voltage states. This switching produces excess voltage noise which can seriously degrade the performance of the SQUID.

Before discussing the numerical methods and the simulations it is instructive to carry out a simple linear circuit analysis of the lumped-circuit-element model. This can easily be done by replacing the nonlinear Josephson junctions by a current source; the junction capacitances and shunt resistances remain. Resonances appear in the form of large amplitude oscillations of the circulating current. The resonant frequencies are determined by the condition that $Im(\bar{Z}_{AB}) = 0$, where \bar{Z}_{AB} is the complex impedance between points A and B marked in Fig. 1(c).

The real and imaginary parts of \bar{Z}_{AB} for $C=1$ pF, $C_p=10$ pF and $R=5$ Ω are shown in Figs. 2(a) and 2(b). In Fig. 2(a), $L=40$ pH and $L_p=0$. A single low-frequency resonance determined by L and C_p occurs at 7.6 GHz. In Fig. 2(b), $L=30$ pH and $L_p=10$ pH. The low-frequency resonance moves up to 8.9 GHz and an additional high-frequency resonance determined by L_p and C appears at 72.9 GHz. The Q value of the high-frequency resonance is lower than that for the low-frequency resonance because of the damping effect of the shunt resistors on the high-frequency resonance. Nevertheless, this simple analysis suggests that, at high frequencies where C_p short circuits

the SQUID loop inductance, the SQUID dynamics may become sensitive to the parasitic inductance and the junction capacitance if $L_p \neq 0$. We will show in Sec. III that this indeed is the case.

III. NUMERICAL RESULTS

The goal of the numerical simulations is to determine how the parasitic elements C_p and L_p influence the SQUID characteristics and noise performance. Numerical calculations which include the effects of the Josephson junction capacitance ($\beta_c \neq 0$) and thermal noise are very time consuming. In order to calculate the average voltage across the SQUID and the voltage noise spectral density, the instantaneous voltage must be integrated over thousands of Josephson periods because of the existence of multiple voltage states. For this reason, it is not possible to carry out simulations as a function of all the SQUID parameters. We therefore consider a set of technologically reasonable SQUID parameters and vary the ratios C_p/C and L/L_p . The results should be qualitatively valid for a large range of SQUID parameters.

A. Numerical methods

The differential equations presented in Sec. II can be solved numerically. We use a fourth-order Runge-Kutta routine⁴⁷ in a vectorized FORTRAN 77 program that runs on an IBM System/370 mainframe computer to solve the differential equations; alternatively, a Turbo Pascal version runs on an IBM personal computer with an INTEL 80486 processor and graphics interface. The noise terms $i_{n,v}$, $i_{n,\varphi}$, and $i_{n,damp}$ are approximated by assuming that they are constant over the time interval Δt^* . The uncorrelated values of the Gaussian distributed random variables are thus time averages of noise terms over Δt^* with zero mean. The variance of the random numbers is $\Gamma/\Delta t^*$ for $i_{n,v}$ and $i_{n,\varphi}$, and $\rho\Gamma/\Delta t^*$ for $i_{n,damp}$. The time intervals Δt^* are chosen such that $\Delta t^* \lesssim \Gamma$.^{39,40}

The average voltage \bar{V} across the SQUID is calculated from the relation $\bar{V} = \Phi_0 f_J$, where f_J is the Josephson frequency. In dimensionless form the average voltage is

$$\bar{v} = \bar{V}/RI_c = N \cdot 2\pi / \sum_{i=1}^N \Delta t_i^*, \quad (5)$$

where Δt_i^* is the time which the system needs to move over one period of the Josephson oscillation. The time intervals Δt_i^* are accurately calculated by applying a Newton-Raphson iteration after the integration step exceeds a period of 2π . The number of periods N is chosen so that the total time is much longer than the longest time constant for the switching processes between different voltage states.^{39,40} Depending on the parameter range, 4000–40 000 Josephson periods are averaged.

To calculate the voltage noise spectrum, a sequence of 2^{15} – 2^{18} intervals Δt_i^* is stored. The corresponding voltage sequence $\bar{v}_i = 2\pi/\Delta t_i^*$ is sampled at equal time intervals $\pi/(\bar{v}_i)_{\max}$, where $(\bar{v}_i)_{\max}$ is the highest average voltage. The sampling frequency is thus twice the highest frequency to avoid the alias effect. The voltage noise power spectral

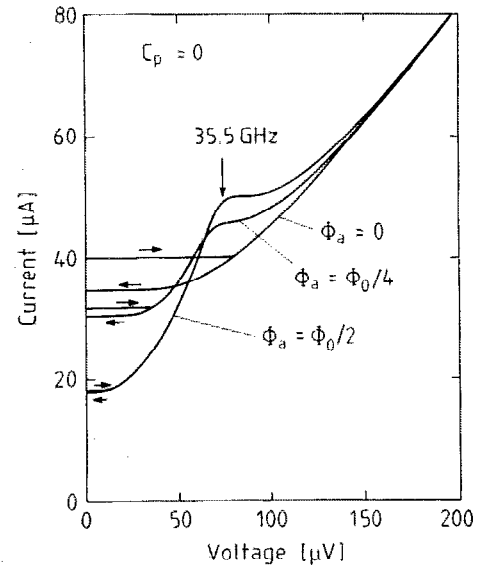


FIG. 3. Noise-free current-voltage characteristics of a dc SQUID with $L_{\text{tot}} = L + L_p = 40$ pH, $L_p = 0$, $I_c = 20$ μ A, $C = 1$ pF, and $R = 5$ Ω for $\Phi_a = 0$, $\Phi_0/4$, and $\Phi_0/2$. The direction of the hysteresis loops is indicated by arrows.

density is calculated by averaging a total of 4–16 FFT spectra of 32 768 data points. The minimum of the frequency is thus 3×10^{-5} times the sampling frequency, or about 1–5 MHz for our parameter range.

B. Calculated current-voltage characteristics

We have chosen the parameters for the simulations to be similar to those of the experimental test devices to be described in Sec. IV A. For all of the calculated characteristics discussed below, the total SQUID inductance $L_{\text{tot}} = 40$ pH, the junction capacitance $C = 1$ pF, the critical current $I_c = 20$ μ A, and the shunt resistance $R = 5$ Ω ; only the ratios C_p/C and L/L_p are varied. The corresponding values for the dimensionless parameters are $\beta_L = 2.43$ and $\beta_c = 1.52$.

In order to more clearly see how the multiple voltage states emerge, we consider first the noise-free I - V characteristics for $C_p = L_p = 0$ shown in Fig. 3. For all values of Φ_a , the transition to the finite voltage state is hysteretic. The direction of the hysteresis loops is indicated by small arrows. For $\Phi_a = 0$, the hysteresis separates the zero-voltage state from the finite running mode; the beating mode is not present. For $\Phi_a \neq 0$, the characteristics for $\Phi_a = \Phi_0/4$ and especially for $\Phi_a = \Phi_0/2$ exhibit the formation of a current step at about 70 μ V or 34 GHz. This agrees very well with the resonant frequency of 35.5 GHz (arrow) calculated using a linear circuit analysis and the values of L and $C/2$. The large amplitude current oscillations at the resonance are indicative of the beating mode, and therefore the V - Φ characteristic for $\Phi_a = \Phi_0/2$ is most sensitive to this feature. For this particular choice of parameters, the transition region between the beating mode and the running mode is nonhysteretic so the two cannot be easily distinguished. We loosely identify that portion of

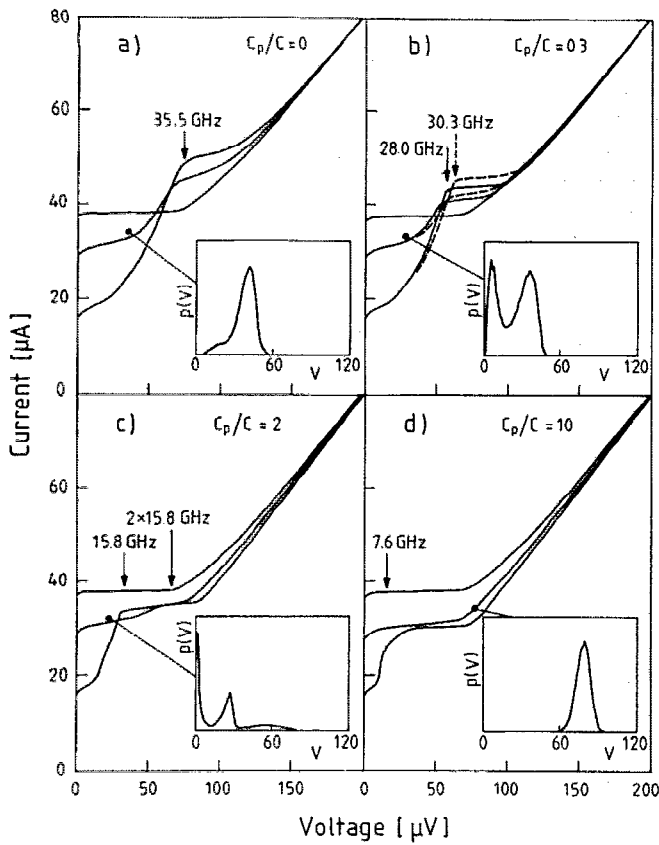


FIG. 4. Calculated current-voltage characteristics for $L_{\text{tot}} = L + L_p = 40$ pH, $L_p = 0$, $I_c = 20$ μ A, $C = 1$ pF, $R = 5$ Ω , and (a) $C_p/C = 0$, (b) $C_p/C = 0.3$, (c) $C_p/C = 2$, and (d) $C_p/C = 10$. The optimal points of operation are indicated by solid circles, and the insets show the probability distribution of the voltage at the indicated points of operation. In (b), the dashed lines are the characteristics for the same parameters except $L/L_p = 3$.

the characteristic below the current step as the branch corresponding to the beating mode, and the portion well above the step as the branch corresponding to the running mode.

We now consider the I - V characteristics in the presence of thermal noise. For all simulations, $\Gamma = 0.0088$. We show the characteristics for $L_p = 0$ ($L_{\text{tot}} = L = 40$ pH) and several values of C_p/C in Fig. 4, and the characteristics for different values of L/L_p and C_p/C in Fig. 5. For each set of parameters, the characteristics for $\Phi_a = 0$, $\Phi_0/4$, and $\Phi_0/2$ are shown. In both figures, the resonant frequencies calculated using a linear circuit analysis of the lumped-circuit-element model, as discussed in Sec. II, are indicated by solid arrows. In some cases, the second harmonics of these resonances are also indicated. The locations of the resonances calculated in this way are seen to be in very good agreement with features in the I - V characteristics for $\Phi_a = \Phi_0/2$. In addition, for each set of I - V characteristics, a point of operation where the calculated energy resolution is near the minimum is marked by a solid circle, and the probability distribution of the voltage at this point of operation is shown in an inset. The probability distribution provides additional insight into the dynamics of the system. The appearance of several peaks in the probability

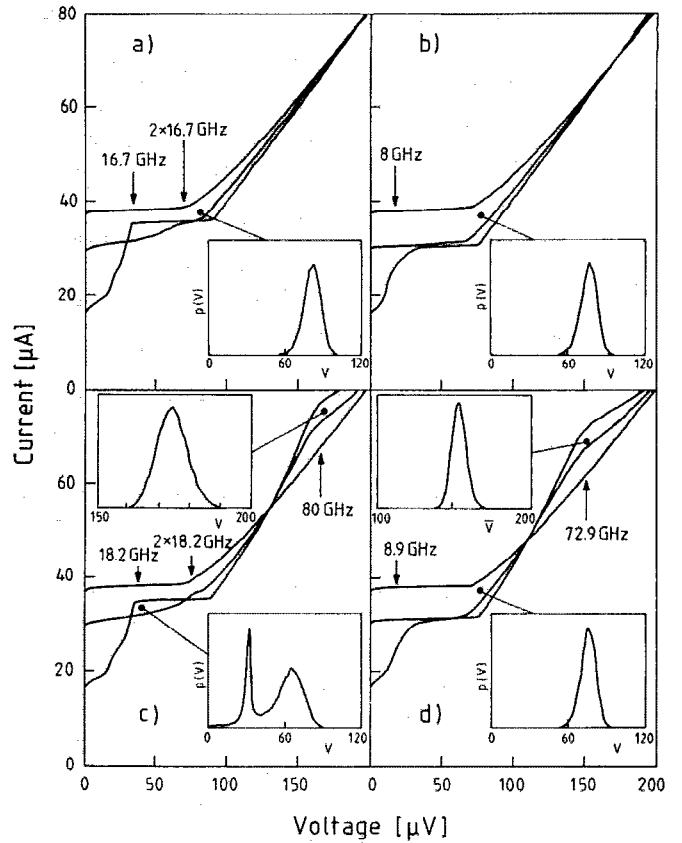


FIG. 5. Calculated current-voltage characteristics for $L_{\text{tot}} = L + L_p = 40$ pH, $I_c = 20$ μ A, $C = 1$ pF, $R = 5$ Ω , and (a) $L/L_p = 9$, $C_p/C = 2$, (b) $L/L_p = 9$, $C_p/C = 10$, (c) $L/L_p = 3$, $C_p/C = 2$, and (d) $L/L_p = 3$, $C_p/C = 10$. The optimal points of operation are indicated by solid circles, and the insets show the probability distribution of the voltage at the indicated points of operation.

distribution indicates the existence of multiple voltage states. The peak width is a measure of the local stability of the voltage state (a sharp, narrow peak is locally very stable), and the peak height is a measure of the global stability of the state (a very high peak is globally very stable).⁴⁵ Thermal noise can activate hopping transitions from one voltage state to another. On the one hand, these switching events contribute to the voltage noise; on the other hand, they enhance the flux-to-voltage transfer function. This effect will be seen more clearly in Sec. III C.

We present first the characteristics for $L_p = 0$, shown in Fig. 4. This is the case corresponding to the simple approximation discussed in Sec. II.

(i) $C_p = 0$ [Fig. 4(a)]. These are the noise-rounded characteristics corresponding to the noise-free characteristics shown in Fig. 3. The most important effect of the thermal noise is that the hysteresis loops are smeared out and a finite voltage state appears for $I_b < 2I_c$ and $\Phi_a = 0$. With the hysteresis removed, it can be seen that the current step due to the L - $(C/2)$ resonance produces two distinct regions of operation where the voltage modulation with applied flux has opposite polarity. The optimal point of operation for this set of parameters is below the resonance. The SQUID is operating in a beating-type mode,

and the probability distribution shown in the inset indicates that the SQUID is in a single voltage state, although some switching to a lower voltage state occurs.

(ii) $C_p/C = 0.3$ [Fig. 4(b)]. The small parasitic capacitance sharpens the current step and causes it to move to a lower voltage. The optimal point of operation is also pushed to a lower voltage but the SQUID is operating in a beating-type mode. The probability distribution now shows that the SQUID undergoes considerable switching between the zero-voltage state and the beating mode (the peak corresponding to the zero-voltage state occurs at a small finite voltage because of the low-pass filter effect). For comparison, the characteristics for the same parameters except $L/L_p = 3$ are shown by the dashed curves. The inductance is now reduced to $L = (3/4)L_{\text{tot}}$, and the current step occurs at a slightly higher voltage; otherwise, the effect of parasitic inductance on the characteristics for $C_p < C$ is seen to be negligible.

(iii) $C_p/C = 2$ [Fig. 4(c)]. The two distinct regions of operation disappear and a new range of bias currents emerge where the maximum peak-to-peak voltage modulation (voltage swing $\Delta\bar{V}$) is significantly higher. The current step due to the resonance is sharp and moves to a lower voltage. A small feature in the characteristic for $\Phi_a = \Phi_0/4$ can even be seen at the second harmonic of this resonance. The optimal point of operation also moves to a lower voltage where a classification of the mode of operation is difficult. The probability distribution shows that the SQUID is switching between three accessible states: the zero-voltage state, the finite voltage state corresponding to the L - C_p resonance, and the second harmonic of this resonance.

(iv) $C_p/C = 10$ [Fig. 4(d)]. The range of bias currents corresponding to large voltage swing increases, and the current step due to the resonance is rounded but still well defined and occurs at a much lower voltage. Favorable operation below the resonance is no longer possible and the optimal point of operation moves to a much higher voltage, above the resonance, where the SQUID operates in the running mode. The single peak in the probability distribution indicates that there is no switching; the SQUID is operating in a stable state.

We now consider the more general case where $L_p \neq 0$. This is the case corresponding to the T -circuit approximation and the double-loop geometry discussed in Sec. II. The noise-rounded characteristics for two different values of the ratio L/L_p are shown in Fig. 5.

(i) $L/L_p = 9$, $C_p/C = 2$ and 10 [Figs. 5(a) and 5(b), respectively]. For small parasitic inductance, the high-frequency resonance determined by L_p and $C/2$ has a negligible influence on the dynamics. For each value of C_p/C , the optimal point of operation is well above the current step due to the low-frequency resonance which is now determined by L and C_p in parallel with $C/2$. The SQUID is operating in the running mode and the probability distribution of the voltage indicates that the point of operation is stable in each case.

(ii) $L/L_p = 3$, $C_p/C = 2$ and 10 [Figs. 5(c) and 5(d), respectively]. For large parasitic inductance, the resonance

determined by L_p and $C/2$ is now in a frequency range where it can have an impact on the dynamics: a second region of sizable voltage swing appears at high frequencies. In this second or high-frequency region of operation, the optimal operating point is marked by a solid circle and is seen to be very near the resonance calculated using linear circuit analysis in both cases. The probability distributions at the respective points of operation are shown in the insets and indicate that the SQUID is in a stable mode of operation. The fact that the characteristics are very nonhysteretic makes a classification of the mode (beating or running) impossible. In the low-frequency region, the current step is now at a slightly higher voltage in each case because of the decrease of L . For $C_p/C = 2$, the optimal point of operation in the low-frequency region is seen to be very near the current step where, according to the probability distribution of the voltage, switching between the finite voltage state corresponding to the L - C_p resonance and the first harmonic of this resonance occurs. The small width of the peak near $30 \mu\text{V}$ indicates that this state is locally very stable, but thermal noise is sufficient to activate hopping to the higher voltage state. For $C_p/C = 10$, the low-frequency optimal point of operation is well above the current step. The SQUID is operating in the running mode and the probability distribution indicates that the point of operation is stable.

C. Calculated noise performance

In this section, we present the performance data for the case $L/L_p = 3$ and several values of the ratio C_p/C . In Fig. 6, the voltage-flux (V - Φ) characteristics (solid curves), voltage noise $\langle V_n^2 \rangle^{1/2}$ (long dashed curves), flux-to-voltage transfer function (gain) $\partial V / \partial \Phi_a$ (short-dashed curves), and the flux noise $\langle \Phi_n^2 \rangle^{1/2}$ (dot-dashed curves) as functions of the applied flux are shown for $C_p/C = 0.3, 2$, and 10. The bias current for each case is the value at the corresponding point of operation marked in the I - V characteristics.

(i) $C_p/C = 0.3$ [Figs. 6(a) and 6(b)]. The corresponding I - V characteristics are shown in Fig. 4(b). The V - Φ characteristics are smooth and the flux noise has a broad minimum around $\Phi_a = 0.25\Phi_0$. The voltage noise and the gain are seen to be closely correlated: the switching between voltage states increases the flux-to-voltage transfer function. Since $\langle \Phi_n^2 \rangle^{1/2} = \langle V_n^2 \rangle^{1/2} / (\partial V / \partial \Phi_a)$, this means that high gain compensates high $\langle V_n^2 \rangle^{1/2}$. The minimum of $\langle \Phi_n^2 \rangle^{1/2}$ does not occur at the point where the gain is maximum, however, but rather at a point just above the maximum where the voltage noise and the gain, although still high, are reduced.

(ii) $C_p/C = 2$ [Figs. 6(c) and 6(d)]. The corresponding I - V characteristics are shown in Fig. 5(c). Although over 25 000 Josephson periods have been averaged, the calculated V - Φ characteristic has a large variance and appears to be very noisy in the range $\Phi_a \approx (0.35-0.5)\Phi_0$. The same behavior is observed for the voltage noise in the same range of applied flux. Evidently, hopping events between voltage states with extremely long transition times exist in this

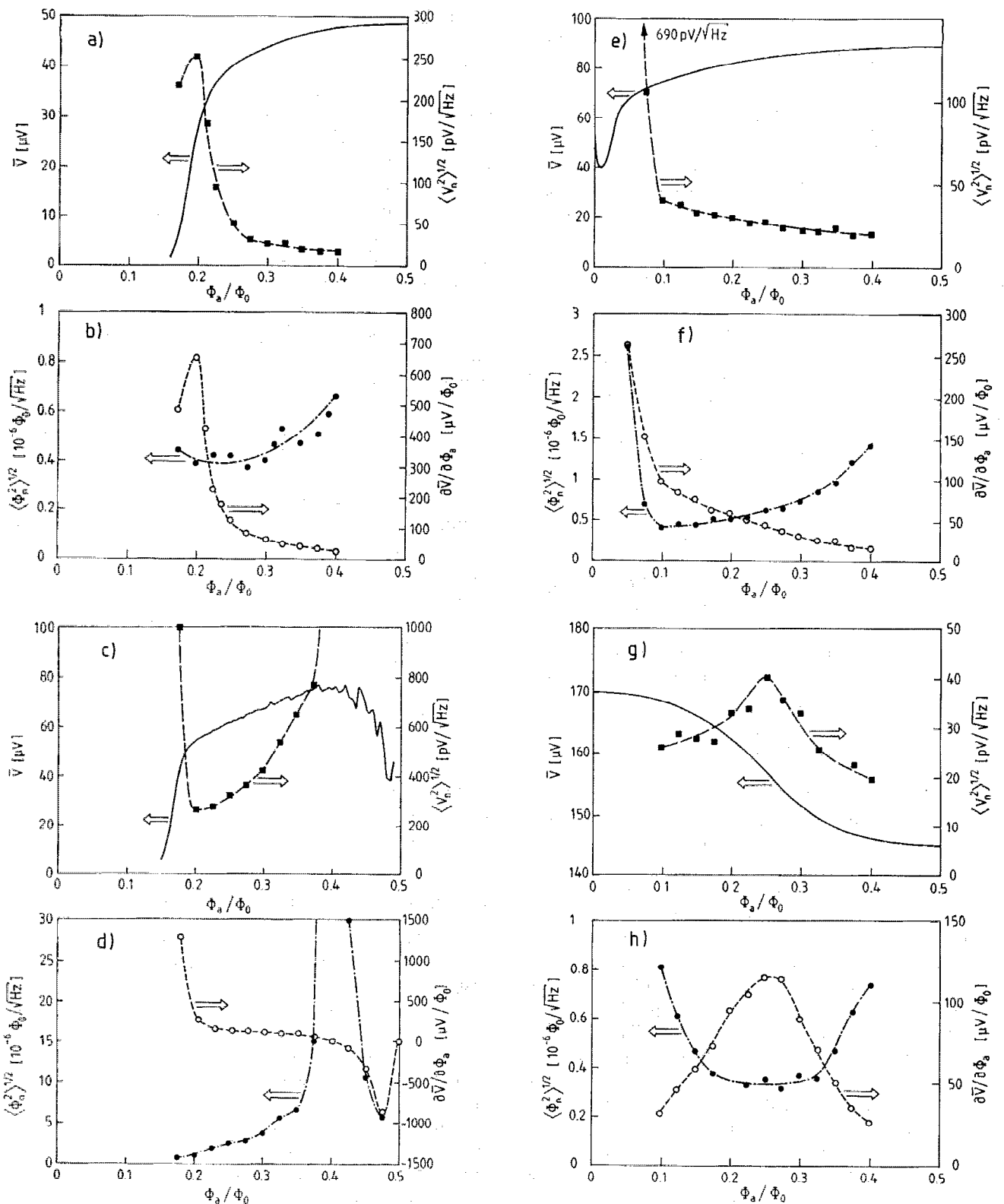


FIG. 6. Calculated average voltage \bar{V} (solid curves), voltage noise V_n (dashed curves), flux-to-voltage transfer function $\partial\bar{V}/\partial\Phi_a$ (short-dashed curves) and the flux noise Φ_n (dot-dashed curves) as a function of applied flux for $L_{\text{tot}} = L + L_p = 40$ pH, $L_s/L = 3$, $I_c = 20$ μA , $C = 1$ pF, $R = 5$ Ω , and (a) and (b) $C_p/C = 0.3$, $I_b = 34$ μA , (c) and (d) $C_p/C = 2$, $I_b = 34$ μA , (e) and (f) $C_p/C = 10$, $I_b = 36$ μA , and (g) and (h) $C_p/C = 10$, $I_b = 70$ μA .

parameter range. The flux noise minimum near $\Phi_a = 0.18 \Phi_0$ is above the point where the gain is maximum, but the voltage noise and the gain are still very high at this point of operation.

(iii) $C_p/C = 10$ [Figs. 6(c)–6(h)]. The corresponding I - V characteristics are shown in Fig. 5(d). For this choice of parameters, the double-loop geometry is evident. In the low-frequency region [Figs. 6(e) and 6(f)], the optimal

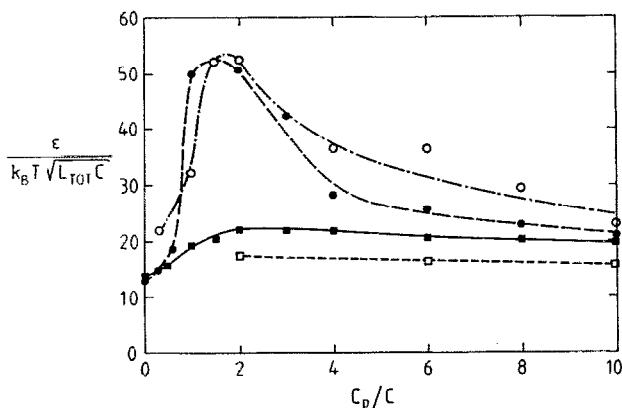


FIG. 7. Calculated normalized energy resolution as a function of C_p/C for $L_{\text{tot}} = L + L_p = 295$ pH, $L_p = 0$, $I_c = 3.5$ μA , $C = 1$ pF, and $R = 8.1$ Ω (solid curve), and for $L_{\text{tot}} = 40$ pH, $I_c = 20$ μA , $C = 1$ pF, $R = 5$ Ω , and $L_p = 0$ (long-dashed curve), $L/L_p = 3$ in the low-frequency region (dot-dashed curve), and $L/L_p = 3$ in the high-frequency region (short-dashed curve).

point of operation is now above the L - C_p resonance. The voltage swing is large and the voltage rise in the V - Φ characteristic for $\Phi_a < 0.1\Phi_0$ is very steep, and the voltage noise, and consequently the gain, are high in this range of applied flux. The minimum flux noise near $\Phi_a \approx 0.1\Phi_0$ is now further above the point of maximum gain in a region where the excess noise due to switching is reduced. The gain at this point of operation is much lower.

The performance data for a point of operation inside the high-frequency resonance [marked by a solid circle in Fig. 5(d)] are shown in Figs. 6(g) and 6(h). In this second region of operation, the voltage swing is reduced but the V - Φ characteristics are smooth and almost sinusoidal. The voltage noise and the gain are again correlated, but now the flux noise minimum occurs at the point of maximum gain. For this particular set of parameters, the flux noise in the high-frequency region is found to be slightly lower than that at the optimal point of operation in the low-frequency region. This simulation result is in good agreement with several experimental results.^{9-12,25,26}

From the above simulations, it is seen that the optimum energy resolution depends both on the parasitic capacitance and inductance. In order to see this dependence more clearly, we have carried out an optimization of the energy resolution as a function of the ratio C_p/C for $L_p = 0$ and $L/L_p = 3$. The other parameters are the same as those given in Sec. III B. For each point, Φ_a and the bias current are varied to find the minimum of the energy resolution. Since two regions of operation exist for the double-loop geometry, separate minima have been found for each region. The normalized optimum energy resolution determined in this way is shown in Fig. 7 for $L_p = 0$ (long-dashed curve), and for $L/L_p = 3$, in the low-frequency region (dot-dashed curve) and in the high-frequency region (short-dashed curve). In addition, the same optimization has been carried out for $L_{\text{tot}} = L = 294$ pH ($L_p = 0$) and $I_c = 3.5$ μA , so that $\beta_L = \pi$ and $\Gamma = 0.05$, and $C = 1$ pF with

$R = 8.1$ Ω so that $\beta_c = 0.7$. Simulations using these values for the dimensionless parameters are often seen in the literature. The results are shown by the solid curve in Fig. 7.

The simulations show that the energy resolution for points of operation in the low-frequency region at first deteriorates as C_p/C increases, but then improves as C_p/C becomes very large. For $L_p = 0$ and $\beta_c = 0.7$ (solid curve), the dependence is approximately $\epsilon \propto \sqrt{L_{\text{tot}}(C + 2C_p)}$ for $C_p/C \lesssim 2$; for $C_p/C > 2$, ϵ saturates and improves slightly to a value that is less than twice that for $C_p/C \approx 0$. The behavior for high β_c is even more dramatic. This effect can be explained by the behavior shown in Fig. 4. As C_p/C becomes large, the optimal point of operation moves to a point well above the L - C_p resonance, where the excess noise due to switching is substantially reduced. The additional capacitance also decreases the noise bandwidth which reduces the mixing-down effect of noise.

Since $\langle \Phi_n^2 \rangle^{1/2} \propto \sqrt{\epsilon}$, the dependence of the flux noise on C_p/C is very weak and can be seen only from very careful measurements. In a previous paper,²³ we presented preliminary noise measurements on similar test devices and the results for $C_p/C \lesssim 2$ are in good agreement with the simulations for $\beta_c = 0.7$, shown in Fig. 7. The previous measurements, however, were carried out manually only at points of operation below the low-frequency L - C_p resonance corresponding to high gain. Thus, the improvement of the energy resolution as C_p/C becomes large could not be seen.

A particularly interesting effect is seen for a point of operation in the high-frequency region: The energy resolution inside the high-frequency resonance for $L/L_p = 3$ is almost independent of C_p/C . The minimum energy resolution found in this case, $\epsilon \approx 15k_B T \sqrt{L_{\text{tot}} C}$, is in good agreement with the results reported by Tesche,⁸ which were calculated in the limit $\beta_c \approx 0$.

D. Effect of additional resistive damping

Damping circuits can be used to improve irregular dc SQUID characteristics. Two simple schemes have been proposed: a resistor-capacitor shunt across the input coil^{14,20,22,26} or simply a resistive shunt in parallel with the SQUID loop.^{10,11,27-30} Both schemes are easy to integrate on a chip and improve the characteristics. The effect is clear but the interaction with the dynamics has not been studied.

In Fig. 8(a), the noise-free characteristics for $L/L_p = 3$ and $C_p/C = 10$ are shown. For $\Phi_a = \Phi_0/2$, the current step due to the L - C_p resonance is very sharp and the beating branch of the characteristic can now be clearly seen. The transitions between the zero-voltage state and the beating mode, as well as between the beating and running modes, are hysteretic. The effect of resistive damping is shown in Fig. 8(b), where the low-frequency resonance is seen to be completely damped by $R_p = 0.1R$. The characteristics, however, remain hysteretic. The origin of the large hysteresis in the characteristics can be understood as follows: In the zero-voltage mode, the inductance is $L_{\text{tot}} = L + L_p$, whereas at high frequencies where C_p short

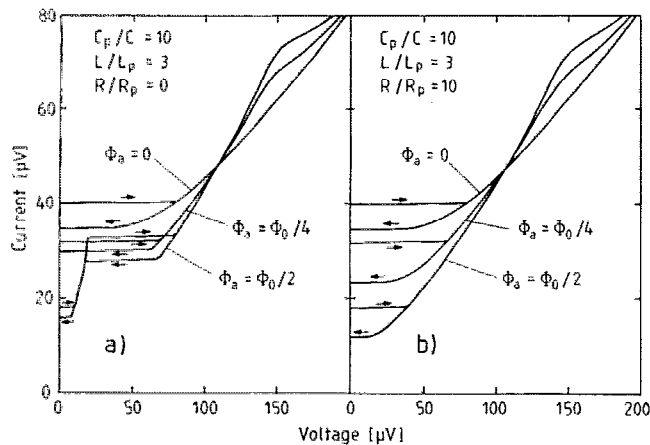


FIG. 8. Noise-free current-voltage characteristics for $L_{\text{tot}} = L + L_p = 40$ pH, $L/L_p = 3$, $C_p/C = 10$, $I_c = 20$ μ A, $C = 1$ pF, $R = 5$ Ω , and (a) $R/R_p = 0$, and (b) $R/R_p = 10$. The direction of the hysteresis loops is indicated by arrows.

circuits the loop inductance L , the effective inductance decreases and $L_{\text{tot}} \approx L_p$. The finite voltage state, therefore, disappears at a different bias current than where it appears. Thus, the hysteresis in Fig. 8(a) has two different origins: the $L C_p$ resonance and the change of the effective SQUID inductance. The high-frequency resonance is nonhysteretic for this set of parameters and the resistive shunt has no effect on the dynamics in this frequency range.

Figure 9 presents the noise-rounded I - V characteristics for $L/L_p = 3$ and $C_p/C = 10$, without (solid lines) and with different values of the damping resistor: $R/R_p = 1$ (short-dashed line), $R/R_p = 0.5$ (dot-dashed line), and $R/R_p = 0.1$ (long-dashed line). For $R/R_p = 0$, thermal noise smears out the hysteresis but the current step due to

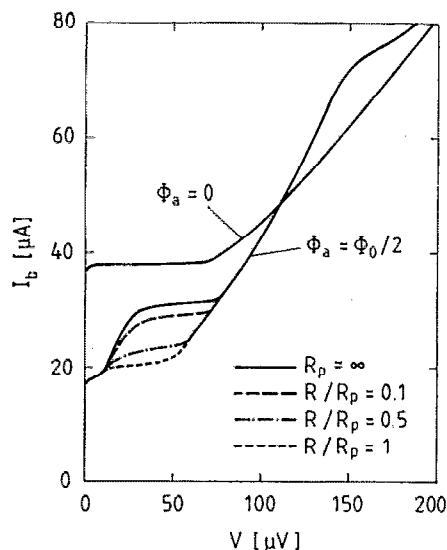


FIG. 9. Calculated current-voltage characteristics for $L_{\text{tot}} = L + L_p = 40$ pH, $L/L_p = 3$, $C_p/C = 10$, $I_c = 20$ μ A, $C = 1$ pF, $R = 5$ Ω , and $R/R_p = 0$ (solid curve), $R/R_p = 0.1$ (long-dashed curve), $R/R_p = 0.5$ (dot-dashed curve), and $R/R_p = 1$ (short-dashed curve).

the low-frequency L - C_p resonance in the characteristic for $\Phi_a = \Phi_0/2$ is still well defined. The resistive shunt effectively removes the resonance and the current step disappears, but the hysteresis in the characteristics, as shown in Fig. 8(b), remains; it is only masked by the thermal smearing. Consequently, the voltage noise is high at bias currents where hopping between the running state and the zero-voltage state occurs.

The corresponding V - Φ characteristics and the flux noise are shown in Fig. 10 for $R/R_p = 0$ (solid lines), $R/R_p = 1$ (dashed lines), and $R/R_p = 10$ (dot-dashed lines). In Figs. 10(a) and 10(b), the bias current is 28 μ A, and in Figs. 10(c) and 10(d), the bias current is 34 μ A. The effect of the low-frequency L - C_p resonance can clearly be seen in Fig. 10(a): the V - Φ characteristic without damping bends towards the resonance for $\Phi_a \approx 0.5 \Phi_0$ (solid curve). The resistive shunt removes the resonant voltage state and the voltage onset is seen to be very sharp for all values of R/R_p . The flux noise shown in Fig. 10(b) improves with damping. In Figs. 10(c) and 10(d), the bias current corresponds to points of operation above the L - C_p resonance and the effect of the damping resistor R_p on the characteristics is small. The noise performance improves slightly, but the best performance is found at points of operations where the gain is low, $\partial V/\partial \Phi_a \approx 100$ μ V/ Φ_0 . For $R/R_p = 1$, the minimum flux noise is comparable to that measured in the high-frequency region shown in Fig. 6(h). If R_p becomes too low, however, the total flux noise will increase because of the current noise contribution from the resistor R_p .

IV. EXPERIMENTS

In this section, we present the results of extensive experimental measurements on several different test devices. We also show the simulated I - V characteristics of these devices that have been calculated using the lumped-circuit-element model described in Sec. II. It is shown that the inclusion of the parasitic inductance in this simple model leads to good agreement between the calculated characteristics and the measurements. The effect of parasitic capacitance and inductance on the performance of the test devices is also discussed.

A. Test devices

The 4×8 mm² test chip contains 11 different test devices. A photograph of one of the test devices is shown in Fig. 11. The SQUIDs are spaced 400 μ m center-to-center from each other. The SQUID inductance is formed by a square washer that is 220 μ m wide with a 20×20 μ m² square hole in the center and a 2–3- μ m-wide slit. The total width of the Nb groundplane which covers the slit ranges from 6–220 μ m. The devices are fabricated using a simple, four-level process⁴⁸ consisting of the following steps: (1) a Nb/Si₃N₄/Nb trilayer is deposited on an entire 2 in. oxidized-Si wafer and patterned using a wet etch, (2) the 20 μ m² Josephson junctions and high critical-current contacts for zero-voltage connections to the base electrode are defined by wet anodization, (3) the Pd shunt resistors are deposited and patterned using lift-off, and (4) a Nb film is

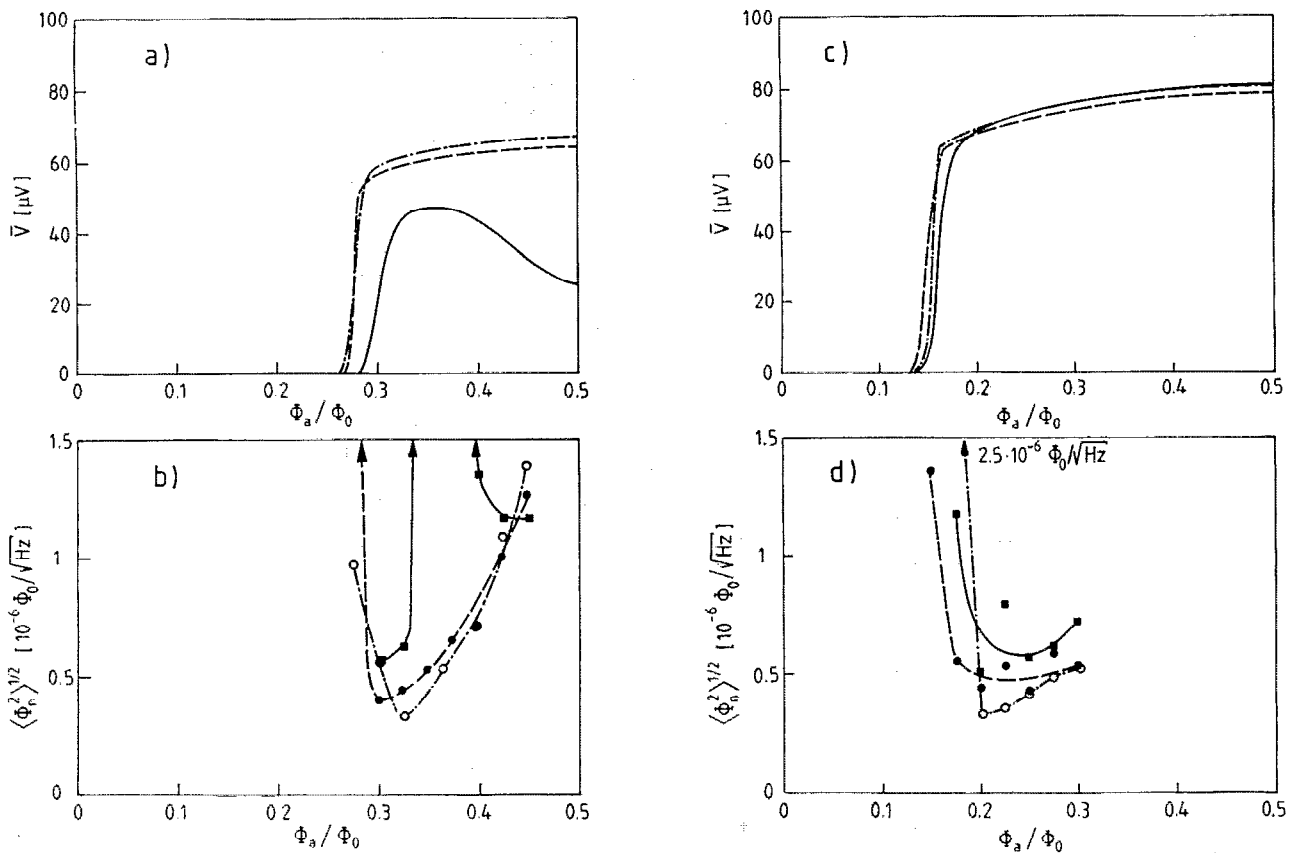


FIG. 10. Calculated average voltage and flux noise as functions of applied flux for $L_{\text{tot}} = L + L_p = 40$ pH, $L/L_p = 3$, $C_p/C = 10$, $I_c = 20$ μ A, $C = 1$ pF, $R = 5$ Ω , and $R/R_p = 0$ (solid curves), $R/R_p = 1$ (dashed curves), $R/R_p = 10$ (dot-dashed curves). (a) and (b) $I_b = 28$ μ A, and (c) and (d) $I_b = 34$ μ A.

deposited to form the slit groundplanes and interconnects and patterned using lift-off.

The test devices are designed so that the total inductance $L_{\text{tot}} \approx 40$ pH. The relatively low inductance ensures that the SQUIDs are not very sensitive to external disturbances. Devices with critical currents ranging from 20 to 30 μ A ($\Gamma \sim 0.01$) have been fabricated and measured. This simplifies the comparison of the simulated characteristics with the measurements because the effects of noise-rounding are not so significant. If the critical current be-

comes too high, however, the simulations become less reliable because of the limited integration times. The junction shunt resistors are designed so that the hysteresis parameter β_c is relatively high. The characteristics in this parameter range are rich in features,²³ which is helpful for the reliable determination of various SQUID electrical parameters and further simplifies the comparison of the simulations with the measurements.

B. Measurement setup

A disadvantage of the small total inductance of the test devices is that the measurements of the flux noise become extremely demanding: for $L_{\text{tot}} = 40$ pH, the magnitude of the flux noise is very low, about $4 \times 10^{-7} \Phi_0 / \sqrt{\text{Hz}}$. Flux noise measurements in the $10^{-7} \Phi_0 / \sqrt{\text{Hz}}$ range can be reliably made using either a low-noise JFET preamplifier with an impedance matching transformer between the SQUID and the preamplifier, or using another dc SQUID as a low-noise preamplifier. Equivalent preamplifier voltage noise levels below 50 pV/ $\sqrt{\text{Hz}}$ can easily be achieved using either method.^{20,23,49-51} If a JFET preamplifier is used, the optimization of the JFET voltage noise requires exact impedance matching to the preamplifier.²¹ The dynamic resistance of the SQUID to be measured, however, can vary by more than a factor of 10 as the point of operation changes.⁵² If a second SQUID is used as a low-noise

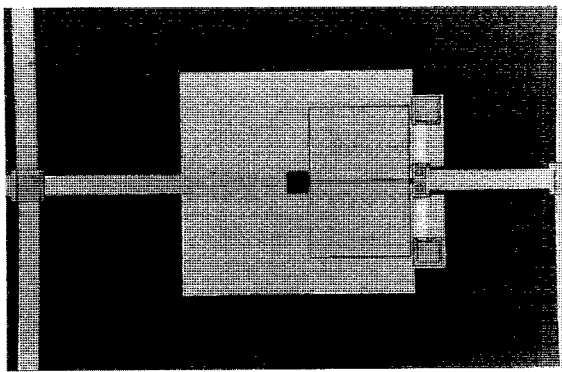


FIG. 11. Photograph of a test device consisting of a square-washer dc SQUID with a superconducting coverplate on top of the slit.

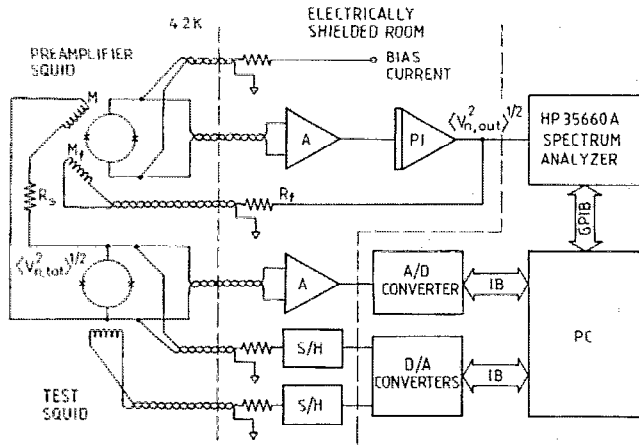


FIG. 12. Schematic diagram of the SQUID measurement system based on a dc SQUID preamplifier. The test SQUID is current and flux biased by signals from the computer, and the noise is measured by a HP 35660A spectrum analyzer that is interfaced to the computer.

preamplifier, the noise contribution of the preamplifier SQUID can change during the noise mapping, but this can easily be checked. In either case, the dynamic resistance has an influence on the measurements and must be measured before subtracting the preamplifier noise contribution.

The subtraction of the preamplifier noise contribution is the most critical issue in determining the intrinsic noise of the test SQUID to be measured, because the intrinsic voltage noise of the test SQUID can be significantly lower than the voltage noise of the preamplifier. The reliability can be enhanced by optimizing the measurement system and by averaging. Concerning the latter, a compromise between the number of different points of operation and the number of averages per point must be made. For the measurements presented here, a complete noise mapping of a given device consists of noise measurements at about 1000 different points of operation and typically requires 3–4 days measurement time.

A schematic diagram of the setup used to measure the dc characteristics and the noise of the test devices is shown in Fig. 12. For the noise measurements, a second dc SQUID²² is used as a low-noise preamplifier. The voltage signal of the test SQUID to be measured is coupled via a wire-wound coil to the preamplifier SQUID. The series resistance of the coil $R_s = 9 \Omega$ and the mutual inductance between the coupling coil and the preamplifier SQUID $M = 1.3 \text{ nH}$. The preamplifier SQUID voltage is amplified using a low-noise bipolar operational amplifier, LT1028, followed by a PI controller. The preamplifier SQUID is operated in flux-locked loop using additional positive feedback.^{10,11,24} The equivalent flux noise of the preamplifier SQUID, $\langle \Phi_{n,1}^2 \rangle^{1/2} = 1.3 \times 10^{-6} \Phi_0 / \sqrt{\text{Hz}}$, is observed to be very stable. The frequency dependence of the output voltage noise is measured with a HP 35660A spectrum analyzer that is computer controlled. The bias current and applied flux for the test SQUID are generated by the computer, and the dc characteristics, the dynamic resistance

R_{dyn} , and the gain $\partial \bar{V} / \partial \Phi_a$ of the test SQUID are measured using a second readout electronics coupled directly to the test SQUID. The noise contribution due to the noise current from the low-noise bipolar preamplifier used in the second readout electronics is negligible.

The total output voltage noise $\langle V_{n,\text{out}}^2 \rangle^{1/2}$ can be written in terms of the total equivalent voltage noise across the test SQUID, $\langle V_{n,\text{tot}}^2 \rangle^{1/2}$, as

$$\langle V_{n,\text{out}}^2 \rangle^{1/2} = \left(\frac{R_f}{R_s + R_{\text{dyn}}} \right) \left(\frac{M}{M_f} \right) \langle V_{n,\text{tot}}^2 \rangle^{1/2}, \quad (6)$$

where R_f is the resistance in the preamplifier SQUID feedback circuit and M_f is the mutual inductance between the feedback coil and the preamplifier SQUID. The total equivalent voltage noise across the test SQUID is given by

$$\langle V_{n,\text{tot}}^2 \rangle^{1/2} = \sqrt{\frac{(R_s + R_{\text{dyn}})^2}{M^2} \langle \Phi_{n,1}^2 \rangle + \left(\frac{\partial V}{\partial \Phi_a} \right)^2 \langle \Phi_{n,2}^2 \rangle + 4k_B T R_s}, \quad (7)$$

where $\langle \Phi_{n,2}^2 \rangle^{1/2}$ is the intrinsic flux noise of the test SQUID and $\sqrt{4k_B T R_s}$ is the noise contribution due to the resistance R_s in the coupling coil. Note that R_{dyn} has to be measured before subtracting the noise contribution of the preamplifier SQUID and the coupling resistor R_s . The measurement system is optimized so that the ratio of the voltage noise $\langle V_{n,2}^2 \rangle^{1/2} = (\partial \bar{V} / \partial \Phi_a) \langle \Phi_{n,2}^2 \rangle^{1/2}$ to the total equivalent voltage noise, $\langle V_{n,2}^2 \rangle^{1/2} / \langle V_{n,\text{tot}}^2 \rangle^{1/2}$, is as large as possible. The flux noise of the preamplifier SQUID is reduced using additional positive feedback,^{10,11,53} and the mutual inductance M is optimized so that the dynamic range of the electronics covers a voltage range of $\pm 300 \mu\text{V}$ across the SQUID under test. For the measurements to be described below, $\langle V_{n,2}^2 \rangle^{1/2} / \langle V_{n,\text{tot}}^2 \rangle^{1/2} \gtrsim 0.3$ for $\langle V_{n,2}^2 \rangle^{1/2} \gtrsim 20 \text{ pV} / \sqrt{\text{Hz}}$.

C. Measured performance

In this section, we summarize the measurements on four different test devices having a range of electrical parameters such that the effects of parasitic capacitance and inductance can clearly be seen. In Fig. 13, the measured I - V characteristics of the four SQUID's for $\Phi_a = 0$, $\Phi_0/2$, and $\Phi_0/4$ are shown as solid curves, and the corresponding simulated characteristics are shown as dotted lines. The simulated characteristics have been calculated using the parameters listed in Table I which are determined in the following way. The junction resistance is calculated from the I - V characteristic for $\Phi_a = 0$ at high bias currents in the usual way. The junction capacitance is derived from measurements on a high β_c , high β_L test device that does not have a slit groundplane. For such a device, the beating mode produces a step in the I - V characteristic for $\Phi_a = 0$ (see Ref. 23). The capacitance is determined by adjusting the parameters in Eqs. (1) and (4) so that the simulated characteristics agree with the measured I - V characteristics. The parasitic capacitance and inductance are estimated, as described in Sec. II. The total inductance is es-

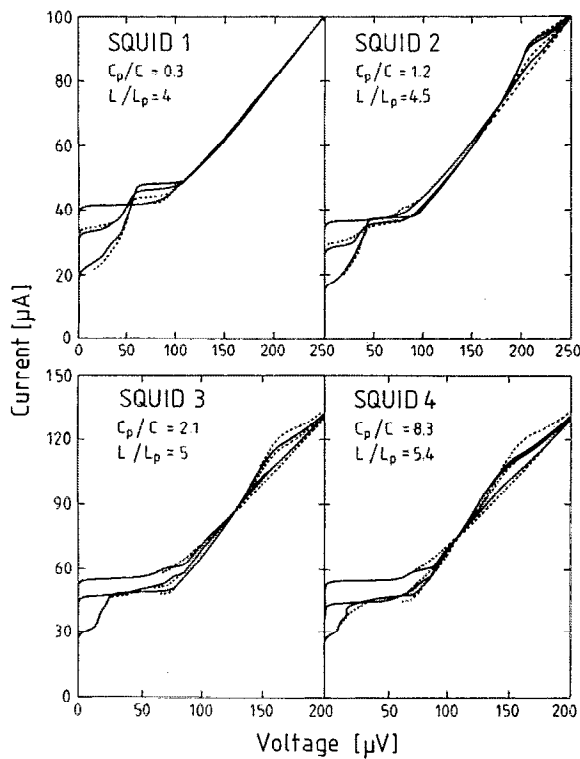


FIG. 13. Measured (solid curves) and calculated (dotted curves) current-voltage characteristics of four different test SQUIDs. The SQUID parameters are listed in Table I.

timated from the measured modulation depth of the critical current.^{54,55} The ratio of the loop inductance L to the parasitic inductance L_p is estimated by comparing the positions of the resonant frequencies calculated using linear circuit analysis, as discussed in Sec. II, with the corresponding features in the measured I - V characteristics. The final values of the parameters in Eqs. (1), (2), and (3) are determined by adjusting them so that the calculated I - V characteristics agree with the measurements.

The I - V characteristics of SQUID 1 are shown in Fig. 13(a). The slit groundplane of this device is narrow so $C_p/C \approx 0.3$. The parameters of this device are comparable to those used to generate Fig. 4(b). The calculated char-

acteristics in Fig. 13(a) agree very well with the measurements, although a feature around $35 \mu\text{V}$ in the characteristic for $\Phi_a = 0$ is not reproduced by the simulations. For this device, $L/L_p \approx 4$, but as shown in Sec. III B, the parasitic inductance has a negligible effect on the I - V characteristics for $C_p/C \lesssim 1$. According to a linear circuit analysis, the high-frequency resonance is above $250 \mu\text{V}$.

For the other three test devices, particularly SQUIDs 3 and 4, the parasitic capacitance is much higher, and a second, high-frequency region of operation due to the L_p -($C/2$) resonance appears at high-bias currents. This resonance can be seen in the I - V characteristics of SQUID's 2, 3, and 4 shown in Figs. 13(b), 13(c), and 13(d), respectively. The calculated characteristics reproduce this feature very well. This would not be the case if the parasitic inductance were neglected. The slight disagreement for high-bias currents may in part be due to self-coupling of the flux from the current leads. The parameters of SQUIDs 2, 3, and 4 are comparable to those used to generate the simulated characteristics shown in Fig. 4(b) and Figs. 5(c) and 5(d), respectively.

We now present the measured performance data for two of the test devices, SQUIDs 1 and 4. As in Sec. III C, the V - Φ characteristics (solid curves), voltage noise (long dashed curves), flux-to-voltage transfer function (short dashed curves), and flux noise (dot-dashed curves) are shown as functions of applied flux in Fig. 14.

For SQUID 1, the measurements performed for bias current $I_b = 28 \mu\text{A}$ are shown in Figs. 14(a) and 14(b), and for $I_b = 36 \mu\text{A}$ in Figs. 14(c) and 14(d). For both bias currents the voltage noise and the gain are seen to be correlated, and the minimum flux noise is measured slightly above the point of maximum gain. At the optimal point of operation for each bias current, the gain is very high: $\partial V/\partial \Phi_a \approx 500 \mu\text{V}/\Phi_0$. These results for SQUID 1 are very similar to the simulation results shown in Figs. 6(a) and 6(b).

For SQUID 4, the measurements for $I_b = 41 \mu\text{A}$ are shown in Figs. 14(e) and 14(f), and for $I_b = 54 \mu\text{A}$ in Figs. 14(g) and 14(h). For $I_b = 41 \mu\text{A}$, the operation of the SQUID is below the L - C_p resonance for all values of applied flux. The voltage noise and the gain are again correlated, and the minimum flux noise is measured just above

TABLE I. The electrical parameters and performance of four uncoupled dc SQUIDs.

Parameter	SQUID 1	SQUID 2	SQUID 3	SQUID 4
Total inductance $L + L_p$	40 pH	38 pH	35 pH	33 pH
Inductance ratio L/L_p	4	4.5	5	5.4
Junction capacitance C	1 pF	1 pF	1.8 pF	1.8 pF
Parasitic capacitance C_p	0.3 pF	1.2 pF	3.8 pF	15 pF
Shunt resistance R	5.1 Ω	5.1 Ω	3.1 Ω	3.1 Ω
Critical current I_c	22 μA	19.5 μA	30 μA	30 μA
$\beta_L = 2\pi L_{\text{tot}} I_c / \Phi_0$	2.7	2.3	3.2	3.0
$\beta_C = 2\pi R^2 C I_c / \Phi_0$	1.7	1.5	1.6	1.6
$\Gamma = 2\pi k_B T / I_c \Phi_0$	0.008	0.009	0.006	0.006
$\langle \Phi_n^2 \rangle_{\text{min}}^{1/2} / \mu\Phi_0 / \sqrt{\text{Hz}}$	0.4	0.45	0.39	0.4
Optimal $(\partial V/\partial \Phi_a)_{\text{opt}}$	500 $\mu\text{V}/\Phi_0$	500 $\mu\text{V}/\Phi_0$	100 $\mu\text{V}/\Phi_0$	100 $\mu\text{V}/\Phi_0$
Optimal \bar{V}	15 μV	14 μV	70.5 μV	69 μV

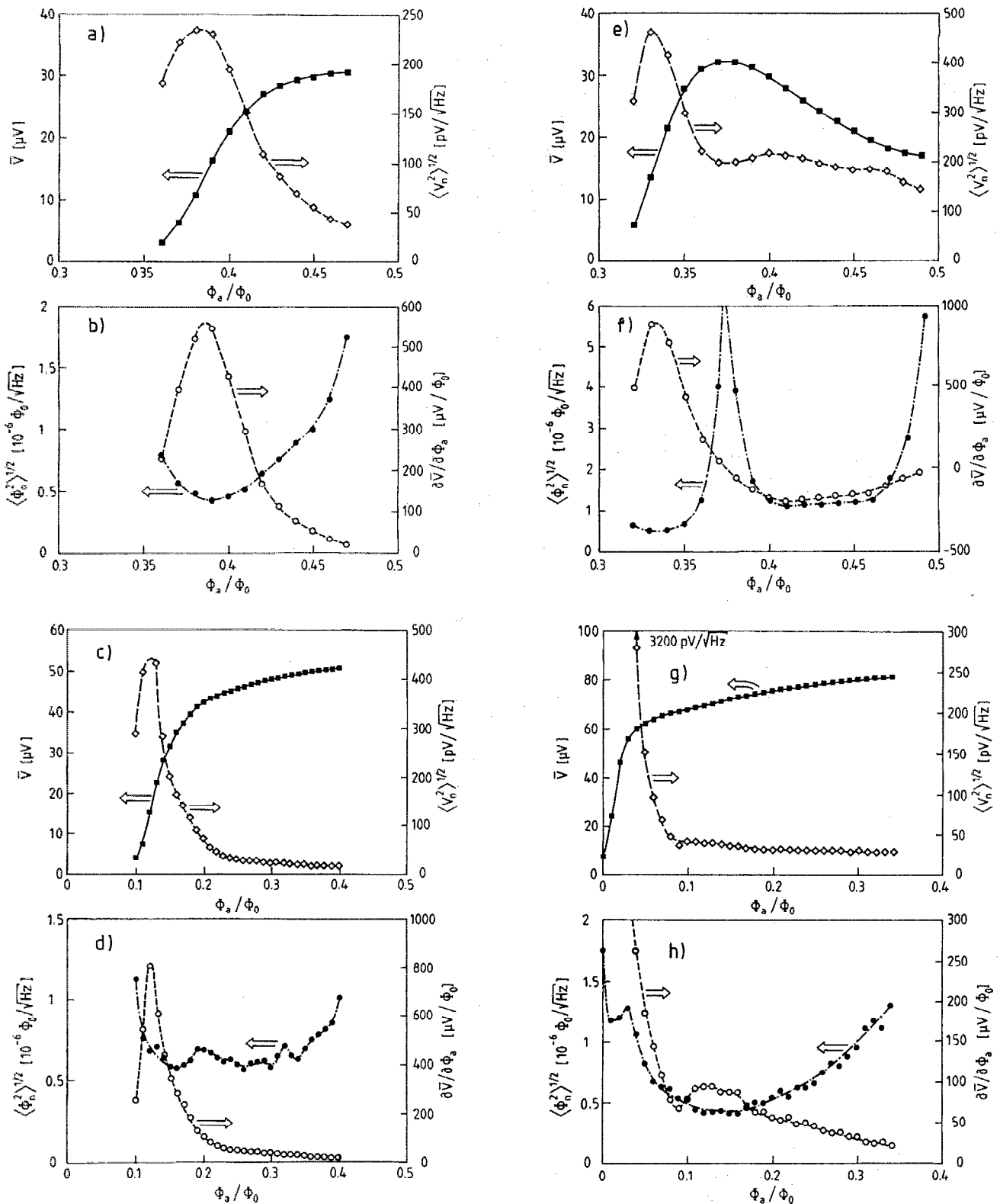


FIG. 14. Measured average voltage \bar{V} (solid curves), voltage noise V_n (dashed curves), flux-to-voltage transfer function $\partial \bar{V} / \partial \Phi_a$ (short-dashed curves), and flux noise Φ_n (dot-dashed curves) as functions of applied flux, for SQUID 1 and bias currents (a) and (b) $I_b = 28 \mu\text{A}$, and (c) and (d) $I_b = 36 \mu\text{A}$, and for SQUID 4 and bias currents (e) and (f) $I_b = 36 \mu\text{A}$, and (g) and (h) $I_b = 70 \mu\text{A}$.

the point of maximum gain. The gain at this point of operation is around $700 \mu\text{V}/\Phi_0$. For $I_b = 54 \mu\text{A}$, the operation of the SQUID is above the L - C_p resonance for all values of applied flux. The voltage noise and the gain are

still correlated, but the minimum flux noise is measured well above the point of maximum gain. The minimum flux noise at this point of operation is lower than that measured at the optimal point for $I_b = 41 \mu\text{A}$, and the gain is now

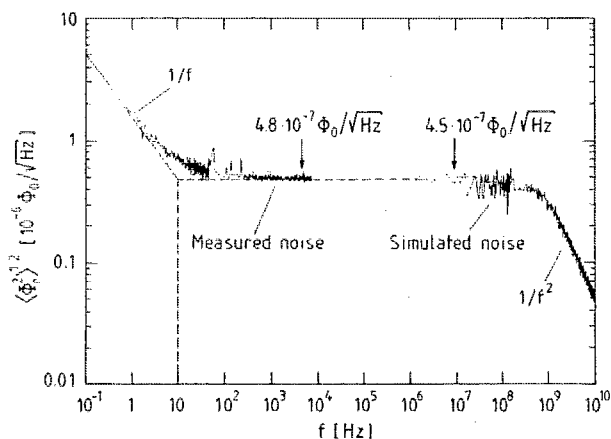


FIG. 15. Equivalent flux noise power spectral density of SQUID 1 for $\Phi_a = 0.38 \Phi_0$ and $I_b = 28 \mu\text{A}$. The low-frequency portion (0.1 Hz–8 kHz) is the measured noise of the SQUID, and the high-frequency portion (above 1 MHz) is the corresponding simulated noise spectrum.

only about $100 \mu\text{V}/\Phi_0$. The results for $I_b = 54 \mu\text{A}$ are similar to the simulation results presented in Figs. 6(e) and 6(f).

The measured and calculated flux-noise power-density spectra of SQUID 1 for $\Phi_a = 0.38 \Phi_0$ and $I_b = 28 \mu\text{A}$ are shown in Fig. 15. The noise has been measured from 0.1 Hz to 8 kHz and calculated for the range 2 MHz to 10 GHz. The $1/f$ noise corner frequency for the measured noise is 10 Hz, and the white noise at 5 kHz (indicated by an arrow) is $4.8 \times 10^{-7} \Phi_0 / \sqrt{\text{Hz}}$. The calculated noise level is slightly lower and has a Lorentzian form with a corner frequency at about 300 MHz. The Lorentzian spectrum is created by the switching process between the zero-voltage state and the beating mode. The white noise is calculated at about 10 MHz by averaging over several frequencies above the Lorentzian corner frequency. For all of the measurements we have made thus far, the measured white flux noise is typically 5%–10% higher than the calculated noise, except when $C_p/C \sim 2$. Possible explanations are that external disturbances contribute excess noise, or the calculated spectra do not include the events with the longest mean switching times, or both. When $C_p/C \sim 2$, the measured flux noise above the L - C_p resonance is found to be clearly lower than the simulated one. In this parameter range, the performance is dominated by excess noise, and the dynamics is very sensitive to external circuits.

In order to see the effect of parasitic capacitance on the energy resolution more clearly, complete noise mappings of all four SQUIDs have been carried out in the low-frequency region ($\bar{V} \lesssim 80 \mu\text{V}$). The mappings are performed with bias current steps of $1 \mu\text{A}$ and applied flux steps of $0.01 \Phi_0$. For each SQUID, the absolute minimum energy resolution in the low-frequency region as a function of \bar{V} has been extracted from the noise mapping data. The results are shown in Fig. 16. Since SQUID's 1 and 2 have relatively low C_p , the minimum energy resolution of both devices is measured below the L - C_p resonance and the optimal point of operation in each case corre-

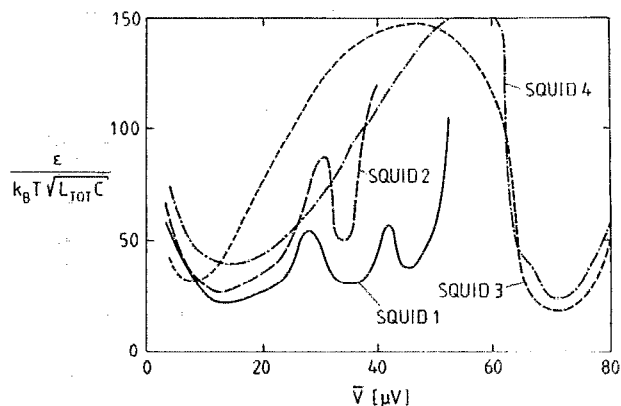


FIG. 16. (a) Measured minimum normalized energy resolution in the low-frequency region ($\bar{V} \lesssim 80 \mu\text{V}$) as a function of the average voltage \bar{V} for SQUID 1 (solid curve), SQUID 2 (long-dashed curve), SQUID 3 (short-dashed curve), and SQUID 4 (dot-dashed curve).

sponds to a low value of \bar{V} , about $15 \mu\text{V}$. For SQUID's 3 and 4, on the other hand, C_p is much higher and the optimal point of operation for each device moves to a frequency well above the L - C_p resonance where the switching between voltage states is reduced. For both devices, \bar{V} is much higher, about $70 \mu\text{V}$. Operation below the resonance ($\bar{V} \approx 10$ – $15 \mu\text{V}$) is possible, but the performance is nearly a factor of 2 worse. The parameters of these devices are such that the minimum energy resolution of SQUIDs 3 and 4 for operation above the L - C_p resonance is actually comparable to that of SQUID 1 for operation below the resonance.

The flux-to-voltage transfer function, however, is very different at the respective optimal points of operation. This effect is seen more clearly in Fig. 17, where the same noise mapping data has been used to plot the minimum energy resolution as a function of gain. Here it can be seen very clearly that, at the optimal points of operation for SQUIDs

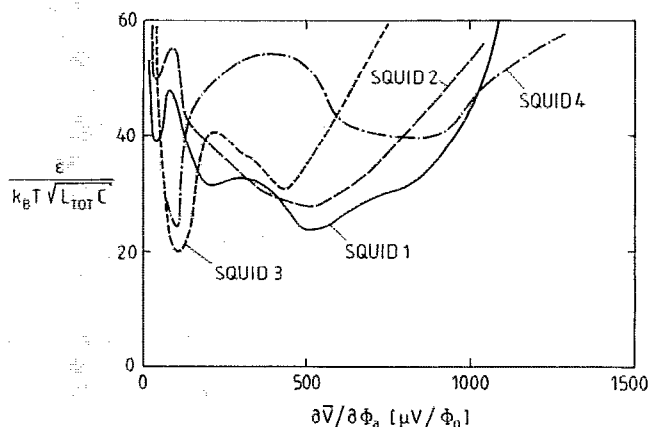


FIG. 17. Measured minimum normalized energy resolution in the low-frequency region ($\bar{V} \lesssim 80 \mu\text{V}$) as a function of the flux-to-voltage transfer function $\partial \bar{V} / \partial \Phi_a$ for SQUID 1 (solid curve), SQUID 2 (long-dashed curve), SQUID 3 (short-dashed curve), and SQUID 4 (dot-dashed curve).

1 and 2, the gain is very high, $\partial\bar{V}/\partial\Phi_a \approx 500 \mu\text{V}/\Phi_0$, whereas for SQUIDS 3 and 4, the gain at the optimal points of operation is lower, $\partial\bar{V}/\partial\Phi_a \approx 100 \mu\text{V}/\Phi_0$. This is consistent with the simulation results shown in Fig. 7.

V. DISCUSSION AND CONCLUSIONS

The simulations presented in Sec. III show that parasitic capacitance and inductance can have a notable effect on the characteristics and performance of the dc SQUID. The dynamics described by two simple lumped-circuit-element models reveal significantly different behavior if $C_p/C \gg 1$ and L_p is not negligible.

The I - V characteristics of recently reported dc SQUIDS^{23,56} without additional damping circuits have features similar to those shown for $C_p/C \gg 1$ in Fig. 4(d): the characteristic for $\Phi_a = \Phi_0/2$ has a large current step, and the region of large voltage modulation decreases gradually with increasing bias current with no change of polarity. The simulation results presented in Sec. III C suggest that such devices may be favorably operated in a region above the current step due to the L - C_p resonance. Below the resonance, the voltage noise is high because of the switching between voltage states and the gain, although high, is not sufficient to compensate for the excess noise. Above the resonance, the voltage noise is much lower and the energy resolution is nearly the same as that for a device having the same junction parameters and total inductance but with $C_p/C \ll 1$. The flux-to-voltage transfer function is also lower above the resonance, however, which places more stringent requirements on the readout electronics.

The simulations also show that an additional region of operation exists for a double-loop geometry with $C_p/C \gg 1$ and $L/L_p \gtrsim 1$. The device can then be operated in the high-frequency L_p -($C/2$) resonance where the V - Φ characteristics are smooth and almost sinusoidal [see Fig. 6(g)]. Such devices are described by Tesche *et al.*⁹ and Drung *et al.*¹⁰⁻¹² According to the simulations, the energy resolution in this region of operation is almost independent of C_p/C and comparable to that of a device with the same total inductance and $C_p/C \ll 1$. The voltage noise is much lower, but the gain is also reduced. The use of additional positive feedback^{10,11,24} or noise cancellation techniques^{53,57} enhances $\partial\bar{V}/\partial\Phi_a$, thereby enabling practical operation with simple readout electronics. One possible complication is that, for $C_p/C \gg 1$, the dynamics become more sensitive to other disturbances, such as microwave resonances, and the actual noise performance may be worse because of the presence of additional accessible voltage states. In addition, the double-loop geometry is feasible only for SQUIDS with relatively high total inductance.¹² Coupled devices that are optimized in order to achieve energy resolutions near the quantum limit, however, require inductances $L_{\text{tot}} \approx 10 \text{ pH}$.²⁷ For such devices, the division of the SQUID inductance into two loops is not possible. Thus, the minimization of C_p is extremely important for very low inductance SQUIDS.

When a resistor is inserted across the SQUID inductance, the simulations show that the resistive shunt damps

the low-frequency L - C_p resonance and effectively smooths the SQUID characteristics; the simulation results shown in Fig. 9 are in good agreement with the experiment.^{22,29,56} But although the resistive shunt is effective in damping the low-frequency L - C_p resonance, it does not remove the hysteresis owing to the double-loop nature that is masked by thermal smearing, and the excess noise does not disappear.

The experimental measurements confirm the general results of the simulations. Using a simple lumped-circuit-element model which includes the effects of both the parasitic capacitance and inductance, the calculated I - V characteristics are shown to be in very good agreement with the measurements. The dependence of the measured energy resolution presented in Sec. IV C is consistent with the results of the simulations: the minimum energy resolution deteriorates with increasing C_p for $C_p/C \lesssim 2$. The effect, however, saturates. For $C_p/C \gg 1$, the energy resolution ϵ becomes comparable to that for $C_p \sim 0$. At the optimal point of operation for devices with $C_p/C \gg 1$, however, the gain is reduced. The discrepancy between the measured and simulated noise performance when $C_p/C \sim 2$ can arise from the dissipations in the external circuits which are connected to the SQUID. This additional damping may reduce excess noise, and thus the measured flux noise appears to be lower than the simulated one.

Daalmans *et al.*²⁵ report similar noise measurements on devices that are designed with a more clear double-loop geometry. Their results are in very good agreement with the simulations presented in Sec. III: the best performance is measured for points of operation inside the high-frequency resonance which arises from the double-loop geometry. We can interpret the results of Fig. 7 in Ref. 25 on the basis of the simulation results shown in Figs. 6(e)-6(h): the best performance is found at points of operation where the hysteresis due to low-frequency resonance is avoided or inside the high-frequency resonance due to the double-loop geometry. This leads to operation at points where the gain is low, which is also observed in Ref. 25.

In summary, the simulation results and experimental measurements suggest two alternative design approaches for the realization of low-noise dc SQUIDS. Either the amount of parasitic capacitance should be minimized so that $C_p/C \ll 1$, or a clear double-loop geometry with $C_p/C \gg 1$ should be used. If a minimal SQUID inductance is desired in order to achieve a very low-flux noise, however, the division of SQUID inductance into two parts in a controllable fashion may be difficult to achieve. A design based on the minimization of C_p is the best solution for low-inductance devices. For SQUID designs with larger inductance, a clear double-loop geometry provides a good alternative without loss of sensitivity.

ACKNOWLEDGMENTS

Financial support of the SITRA foundation is acknowledged. One of the authors (T.R.) acknowledges support from the Academy of Finland. Another of the authors (R.C.) acknowledges partial support from ERP Contract 2597, and wishes to thank the staff of the Metrology Research Institute, Helsinki University of Technology and

the Technical Research Centre of Finland, for support and hospitality during several enjoyable visits in Helsinki.

- ¹R. F. Voss, R. B. Laibowitz, A. N. Broers, S. I. Raider, C. M. Knoedler, and J. M. Viggiano, *IEEE Trans. Magn.* **MAG-17**, 395 (1981).
- ²M. W. Cromar and P. Carelli, *Appl. Phys. Lett.* **38**, 723 (1981).
- ³D. J. Van Harlingen, R. H. Koch, and J. Clarke, *Appl. Phys. Lett.* **41**, 197 (1982).
- ⁴R. T. Wakai and D. J. Van Harlingen, *Appl. Phys. Lett.* **49**, 593 (1986).
- ⁵J. N. Hollenhorst and R. P. Giffard, *IEEE Trans. Magn.* **MAG-15**, 474 (1979).
- ⁶J. N. Hollenhorst and R. P. Giffard, *J. Low Temp. Phys.* **39**, 477 (1980).
- ⁷H. J. Paik, R. H. Mathews, and M. G. Castellano, *IEEE Trans. Magn.* **MAG-17**, 404 (1981).
- ⁸C. D. Tesche, *J. Low Temp. Phys.* **47**, 385 (1982).
- ⁹C. D. Tesche, K. H. Brown, A. C. Callegari, M. M. Chen, J. H. Greiner, H. C. Jones, M. B. Ketchen, K. K. Kim, A. W. Kleinsasser, H. A. Notarys, G. Proto, R. H. Wang, and T. Yogi, *IEEE Trans. Magn.* **MAG-21**, 1032 (1985).
- ¹⁰D. Drung, R. Cantor, M. Peters, H. J. Scheer, and H. Koch, *Appl. Phys. Lett.* **57**, 406 (1990).
- ¹¹D. Drung, R. Cantor, M. Peters, T. Ryhänen, and H. Koch, *IEEE Trans. Magn.* **MAG-27**, 3001 (1991).
- ¹²D. Drung, in *Superconducting Devices and their Applications, Springer Proceedings in Physics*, edited by H. Koch and H. Lübbig (Springer, Berlin, 1991).
- ¹³D. Drung and W. Jutz, in *SQUID'85, Superconducting Quantum Interference Devices and Their Applications*, edited by H. D. Hahlbohm and H. Lübbig (Walter de Gruyter, Berlin, 1985), p. 807.
- ¹⁴H. Seppä and T. Ryhänen, *IEEE Trans. Magn.* **MAG-23**, 1083 (1987).
- ¹⁵R. Leoni, P. Carelli, and V. Foglietti, *J. Appl. Phys.* **64**, 2527 (1988).
- ¹⁶R. S. Germain, M. L. Roukes, M. R. Freeman, R. C. Richardson, and M. B. Ketchen, in *Proceedings of the 17th International Conference on Low Temperature Physics LT-17*, edited by U. Eckern, A. Schmid, W. Weber, and H. Wühl (North-Holland, Amsterdam, 1984), p. 203.
- ¹⁷J. M. Martinis and J. Clarke, *J. Low Temp. Phys.* **61**, 227 (1985).
- ¹⁸C. Hilbert and J. Clarke, *J. Low Temp. Phys.* **61**, 237 (1985).
- ¹⁹B. Muhlfeider, J. A. Beall, M. W. Cromar, R. H. Ono, and W. W. Johnson, *IEEE Trans. Magn.* **MAG-21**, 427 (1985).
- ²⁰J. Knuutila, M. Kajola, H. Seppä, R. Mutikainen, and J. Salmi, *J. Low Temp. Phys.* **71**, 369 (1988).
- ²¹T. Ryhänen, H. Seppä, R. Ilmoniemi, and J. Knuutila, *J. Low Temp. Phys.* **76**, 287 (1989).
- ²²R. Cantor, T. Ryhänen, D. Drung, H. Koch, and H. Seppä, *IEEE Trans. Magn.* **MAG-27**, 2927 (1991).
- ²³T. Ryhänen, R. Cantor, D. Drung, H. Koch, and H. Seppä, *IEEE Trans. Magn.* **MAG-27**, 3013 (1991).
- ²⁴T. Ryhänen, R. Cantor, D. Drung, and H. Koch, *Appl. Phys. Lett.* **59**, 228 (1991).
- ²⁵G. M. Daalmans, L. Bär, D. Uhl, F. Bömmel, R. Kress, and L. Warze-mann, in *Superconducting Devices and their Applications, Springer Proceedings in Physics*, edited by H. Koch and H. Lübbig (Springer, Berlin, 1992).
- ²⁶J. Knuutila, A. Ahonen, and C. Tesche, *J. Low Temp. Phys.* **68**, 269 (1987).
- ²⁷L. Grönberg, H. Seppä, R. Cantor, M. Kiviranta, T. Ryhänen, J. Salmi, and I. Suni, in *Superconducting Devices and their Applications, Springer Proceedings in Physics*, edited by H. Koch and H. Lübbig (Springer, Berlin, 1992).
- ²⁸M. Matsuda, S. Kuriki, and Y. Nagano, *Jpn. J. Appl. Phys.* **25**, 1188 (1986).
- ²⁹V. Foglietti, R. H. Koch, W. J. Gallagher, B. Oh, B. Bumble, and W. Y. Lee, *Appl. Phys. Lett.* **54**, 2259 (1989).
- ³⁰R. Cantor, D. Drung, M. Peters, H. J. Scheer, and H. Koch, *Supercond. Sci. Technol.* **3**, 108 (1990).
- ³¹K. Enpuku, K. Sueoka, K. Yoshida, and F. Irie, *J. Appl. Phys.* **57**, 1691 (1985).
- ³²J. M. Jaycox and M. B. Ketchen, *IEEE Trans. Magn.* **MAG-17**, 400 (1981).
- ³³M. B. Ketchen and J. M. Jaycox, *Appl. Phys. Lett.* **40**, 736 (1982).
- ³⁴M. B. Ketchen, *IEEE Trans. Magn.* **MAG-23**, 1650 (1987).
- ³⁵D. E. McCumber, *J. Appl. Phys.* **7**, 3113 (1968).
- ³⁶W. C. Stewart, *Appl. Phys. Lett.* **12**, 277 (1968).
- ³⁷K. Enpuku and K. Yoshida, *J. Appl. Phys.* **69**, 7295 (1991).
- ³⁸K. Enpuku, R. Cantor, and H. Koch, *J. Appl. Phys.* **71**, 2338 (1991).
- ³⁹J. Kurkijärvi and V. Ambegaokar, *Phys. Lett. A* **31**, 314 (1970).
- ⁴⁰R. F. Voss, *J. Low Temp. Phys.* **42**, 151 (1981).
- ⁴¹E. Ben-Jacob and Y. Imry, *J. Appl. Phys.* **52**, 6806 (1981).
- ⁴²E. Ben-Jacob, D. J. Bergman, B. J. Matkowsky, and Z. Schuss, *Phys. Rev. A* **26**, 2805 (1982).
- ⁴³E. Ben-Jacob, D. J. Bergman, and Z. Schuss, *Phys. Rev. B* **25**, 519 (1982).
- ⁴⁴J. A. Ketoja, J. Kurkijärvi, and R. K. Ritala, *Phys. Rev. B* **30**, 3757 (1984).
- ⁴⁵R. L. Kautz, *Phys. Rev. A* **38**, 2066 (1988).
- ⁴⁶C. D. Tesche, *J. Low Temp. Phys.* **44**, 119 (1981).
- ⁴⁷W. H. Press, B. P. Flannery, S. A. Teukolsky, and W. T. Vetterling, *Numerical Recipes in Pascal: The Art of Scientific Computing* (Cambridge University, New York, 1989).
- ⁴⁸R. Cantor, D. Drung, M. Peters, and H. Koch, *J. Appl. Phys.* **67**, 3038 (1990).
- ⁴⁹V. Foglietti, M. E. Giannini, and G. Petrocco, *IEEE Trans. Magn.* **MAG-27**, 2989 (1991).
- ⁵⁰M. B. Ketchen, M. Bhushan, S. B. Kaplan, and W. J. Gallagher, *IEEE Trans. Magn.* **MAG-27**, 3005 (1991).
- ⁵¹V. Foglietti, *Appl. Phys. Lett.* **59**, 476 (1991).
- ⁵²T. Ryhänen, H. Seppä, R. Cantor, D. Drung, H. Koch, and D. Veld-huis, in *Superconducting Devices and their Applications, Springer Proceedings in Physics*, edited by H. Koch and H. Lübbig (Springer, Berlin, 1992).
- ⁵³H. Seppä, A. Ahonen, J. Knuutila, S. Simola, and V. Vilkmán, *IEEE Trans. Magn.* **MAG-27**, 2488 (1991).
- ⁵⁴C. D. Tesche and J. Clarke, *J. Low Temp. Phys.* **29**, 301 (1977).
- ⁵⁵R. L. Peterson and C. A. Hamilton, *J. Appl. Phys.* **50**, 8135 (1979).
- ⁵⁶G. M. Daalmans, L. Bär, F. R. Bömmel, R. Kress, and D. Uhl, *IEEE Trans. Magn.* **MAG-27**, 2997 (1991).
- ⁵⁷H. Seppä, in *Superconducting Devices and their Applications, Springer Proceedings in Physics*, edited by H. Koch and H. Lübbig (Springer, Berlin, 1992).